

AD-A265 452

2



NASA Contractor Report 191442

ICASE Report No. 93-11

# ICASE



## EFFECT OF ROTATION RATE ON THE FORCES OF A ROTATING CYLINDER: SIMULATION AND CONTROL

John A. Burns  
Yuh-Roung Ou

NASA Contract Nos. NAS1-18605 and NAS1-19480  
March 1993

Institute for Computer Applications in Science and Engineering  
NASA Langley Research Center  
Hampton, Virginia 23681-0001

Operated by the Universities Space Research Association

DTIC  
ELECTE  
JUN 07 1993  
S E D



~~DISTRIBUTION STATEMENT~~  
Approved for public release  
Distribution Unlimited

National Aeronautics and  
Space Administration

Langley Research Center  
Hampton, Virginia 23681-0001

93-12703



49p

93 6 07 04 8

REPORT DOCUMENTATION PAGE			Form Approved OMB No. 0704-0188	
<small>Public reporting burden for this collection of information is estimated to average 1 hour per response, including the time for reviewing instructions, searching existing data sources, gathering and maintaining the data needed, and completing and reviewing the collection of information. Send comments regarding this burden estimate or any other aspect of this collection of information, including suggestions for reducing this burden, to Washington Headquarters Services, Directorate for Information Operations and Reports, 1215 Jefferson Davis Highway, Suite 1204, Arlington, VA 22202-4302, and to the Office of Management and Budget, Paperwork Reduction Project (0704-0188), Washington, DC 20503.</small>				
1. AGENCY USE ONLY (Leave blank)	2. REPORT DATE March 1993	3. REPORT TYPE AND DATES COVERED Contractor Report		
4. TITLE AND SUBTITLE EFFECT OF ROTATION RATE ON THE FORCES OF A ROTATING CYLINDER: SIMULATION AND CONTROL		5. FUNDING NUMBERS C NAS1-18605 C NAS1-19480  WU 505-90-52-01		
6. AUTHOR(S) John A. Burns Yuh-Roung Ou				
7. PERFORMING ORGANIZATION NAME(S) AND ADDRESS(ES) Institute for Computer Applications in Science and Engineering Mail Stop 132C, NASA Langley Research Center Hampton, VA 23681-0001		8. PERFORMING ORGANIZATION REPORT NUMBER  ICASE Report No. 93-11		
9. SPONSORING/MONITORING AGENCY NAME(S) AND ADDRESS(ES) National Aeronautics and Space Administration Langley Research Center Hampton, VA 23681-0001		10. SPONSORING/MONITORING AGENCY REPORT NUMBER NASA CR-191442 ICASE Report No. 93-11		
11. SUPPLEMENTARY NOTES Langley Technical Monitor: Michael F. Card Final Report		Submitted to Physics of Fluid A		
12a. DISTRIBUTION/AVAILABILITY STATEMENT Unclassified - Unlimited  Subject Category 34, 63		12b. DISTRIBUTION CODE		
13. ABSTRACT (Maximum 200 words) In this paper we present numerical solutions to several optimal control problems for an unsteady viscous flow. The main thrust of this work is devoted to simulation and control of an unsteady flow generated by a circular cylinder undergoing rotary motion. By treating the rotation rate as a control variable we formulate two optimal control problems and use a central difference/pseudospectral transform method to numerically compute the optimal control rates. Several types of rotations are considered as potential controls and we show that a proper synchronization of forcing frequency with the natural vortex shedding frequency can greatly influence the flow. The results here indicate that using moving boundary controls for such systems may provide a feasible mechanism for flow control.				
14. SUBJECT TERMS fluid flow control; optimal control			15. NUMBER OF PAGES 49	
			16. PRICE CODE A03	
17. SECURITY CLASSIFICATION OF REPORT Unclassified	18. SECURITY CLASSIFICATION OF THIS PAGE Unclassified	19. SECURITY CLASSIFICATION OF ABSTRACT	20. LIMITATION OF ABSTRACT	

## ICASE Fluid Mechanics

Due to increasing research being conducted at ICASE in the field of fluid mechanics, future ICASE reports in this area of research will be printed with a green cover. Applied and numerical mathematics reports will have the familiar blue cover, while computer science reports will have yellow covers. In all other aspects the reports will remain the same; in particular, they will continue to be submitted to the appropriate journals or conferences for formal publication.

Accession For	
NTIS	CRA&I <input checked="" type="checkbox"/>
DTIC	TAB <input type="checkbox"/>
Unannounced	<input type="checkbox"/>
Justification	
By	
Distribution /	
Availability Codes	
Dist	Avail and / or Special
A-1	

UNIT 6, JANUARY 1968, 2,

# EFFECT OF ROTATION RATE ON THE FORCES OF A ROTATING CYLINDER: SIMULATION AND CONTROL

*John A. Burns*<sup>1</sup>

Interdisciplinary Center for Applied Mathematics  
Department of Mathematics  
Virginia Polytechnic Institute and State University  
Blacksburg, VA 24061-0531

and

*Yuh-Roung Ou*<sup>2</sup>

Interdisciplinary Center for Applied Mathematics  
Aerospace and Ocean Engineering Department  
Virginia Polytechnic Institute and State University  
Blacksburg, VA 24061-0531

## ABSTRACT

In this paper we present numerical solutions to several optimal control problems for an unsteady viscous flow. The main thrust of this work is devoted to simulation and control of an unsteady flow generated by a circular cylinder undergoing rotary motion. By treating the rotation rate as a control variable we formulate two optimal control problems and use a central difference/pseudospectral transform method to numerically compute the optimal control rates. Several types of rotations are considered as potential controls and we show that a proper synchronization of forcing frequency with the natural vortex shedding frequency can greatly influence the flow. The results here indicate that using moving boundary controls for such systems may provide a feasible mechanism for flow control.

---

<sup>1</sup>This work was supported in part by AFOSR under Grant F-49620-92-J-0078, the National Science Foundation under Grant INT-89-22490, and by the National Aeronautics and Space Administration under Contract Nos. NAS1-18605 and NAS1-19480 while the author was a visiting scientist at the Institute for Computer Applications in Science and Engineering (ICASE), NASA Langley Research Center, Hampton, VA 23681-0001.

<sup>2</sup>This research was supported by the National Aeronautics and Space Administration under NASA Contract Nos. NAS1-18605 and NAS1-19480 while the author was in residence at the Institute for Computer Applications in Science and Engineering (ICASE), NASA Langley Research Center, Hampton, VA 23681-0001, and by AFOSR under Grant F-49620-92-J-0078.

## 1. INTRODUCTION

The benefits received from applying control mechanisms in viscous flows has been long realized since the pioneering work of Prandtl [30]. Because of a growing interest in controlling the behavior and structure of fluid flows, various topics in flow control have recently become a subject of research focus [14, 1, 13, 34, 4, 15, 26, 35, 9, 16, 20, 27, 28, 29, 36]. A potentially important application of flow control is the enhancement of the aerodynamic characteristics of future advanced aircraft. Although recent research has produced a variety of methods to achieve desired performance and design goals for maneuvering vehicles, it is now widely recognized that further gains will most likely come from the application of various types of flow control mechanisms [11, 12]. Consequently, the utility of flow control becomes a critical issue in the design process which may provide real-time effect for many important applications, such as highly instantaneous maneuvers for the super-maneuverable aircraft [18], and the optimum design of aerodynamic configurations [21]. Considerable effort has been devoted to the improvement of control mechanisms. However, the principal progress to-date has been essentially accomplished by experimental investigations, while most analytical and numerical approaches have remained in its infancy due to the complexity of the problems.

One of the most practical applications of control mechanisms in flow systems has been boundary-layer separation control. In this area of research, several methods have been developed experimentally to provide various control mechanisms, for example moving surfaces, blowing, suction, injection of a different gas, etc [31, 32]. In particular, it has been demonstrated in a number of experiments by Modi et al. [25, 24] that moving surfaces can effectively provide boundary-layer control. In their experiments, the boundary-layer flow is controlled by an application of two rotating cylinders located at the leading and trailing edges of an airfoil. It has been shown that this mechanism can prevent flow separation by retarding the initial growth of the boundary layer, with the important consequences of lift enhancement and stall delay. For instance, when the speed ratios (which represents the ratio of cylinder surface speed to the freestream speed) of both cylinders were set at a constant value of 4, the

results indicated a 200% increase of the maximum lift coefficient compared with the reference airfoil (in which no rotating cylinder is attached). In spite of the fact that considerable aerodynamic benefits were gained by changing the cylinder speed ratio, in their experiments the speed of rotation was performed merely with constant values. However, it should be noted that if the rotating cylinder mechanism is applied to a region of unsteady flow, a constant rotation rate may not correspond to the optimal performance when an airfoil is undergoing a rapid maneuver. This type of result provided the motivation for us to consider a fundamental problem regarding unsteady flow control by means of a time-dependent moving surface mechanism. In order to keep the problem reasonable and yet practical, we selected a model for the numerical study of controlling the temporal development of the flow field around a rotating cylinder.

The most distinguishing feature of a rotating body traveling through a fluid is that it experiences a transverse force acting in a direction perpendicular to that of flowing stream [37]. In the past few decades, research on the problem of a uniform stream past a cylindrical rotating body has been the subject of many experimental and numerical investigations. See the papers by Taneda [39], Mo [23] and Tokumaru and Dimotakis [40] for a cylinder undergoing rotary oscillations, Prandtl [31], Taneda [38], Koromilas and Telionis [22], Coutanceau and M  nard [8], Badr and Dennis [3], Badr et al. [2] and Chen et al. [7] for a cylinder with a constant speed of rotation. However, most of these results are primarily focused on the study of formation and development of vortices in a cylinder wake. It appears that the effect of the rotation rate on the cylinder forces exerted by the fluid has received far less attention, despite the fact that it has many important practical engineering applications.

The main thrust of the current investigation is on simulation and control of an unsteady flow generated by a circular cylinder undergoing a combined (steady or unsteady) rotary and rectilinear motion. By treating the rotation rate as a control variable in this model, we consider several problems concerning the temporal development of forces on a rotating cylinder in response to a variety of time-dependent rotation rates. The computational results

provide considerable insight into the problem of controlling such flows.

## 2. MATHEMATICAL AND NUMERICAL FORMULATIONS

In this section the governing equations and the particular numerical method used in this work are described. We consider control problems for a two-dimensional viscous incompressible flow generated by an impulsively started circular cylinder. The cylinder is translated with a constant rectilinear speed  $U$  normal to its generator and is simultaneously rotated with a time-dependent angular velocity  $\tilde{\Omega}(t)$  about its axis. Although there are various formulations and numerical techniques for the solving of steady and unsteady flow past a rotating cylinder [19, 3, 23], in this work the problem is investigated numerically by solving a velocity/vorticity formulation of the Navier-Stokes equations with an implementation of the Biot-Savart law. The numerical approach used in the present study is the one developed by Chen [5] for the problem of a circular cylinder oscillating in a rectangular box. It is based on an explicit finite-difference/pseudo-spectral technique to yield time accurate solutions to the governing equations. This numerical algorithm was further modified to investigate an unsteady flow around a rotating cylinder undergoing various constant rotational speeds [7, 28], and time-dependent rotation rates [26, 27].

Several prominent features in the application of an integral representation for flow kinematics are emphasized in §2.2. This integral method proposed by Wu and Thompson [46] provides the basic link between the velocity and vorticity fields throughout the numerical procedure. The boundary vorticity at the solid surface can be easily calculated by the application of this integral. Moreover, unlike other numerical approaches, the imposition of the artificial far-field boundary condition for the velocity is not necessary once the vorticity values are known everywhere in the domain of interest.

### 2.1 Governing Equations

In the velocity/vorticity formulation of the Navier-Stokes equations, the governing equations consist of the vorticity transport equation and the vector Poisson equation for the veloc-

ity. Thus, for a two-dimensional unsteady viscous flow in incompressible fluid, the Cartesian coordinate form of the governing equations for the vorticity and velocity can be expressed in the dimensionless form as

$$\frac{\partial \omega}{\partial t} + \vec{u} \cdot \nabla \omega = \frac{2}{Re} \nabla^2 \omega \quad (1)$$

and

$$\nabla^2 \vec{u} = -\nabla \times (\omega \vec{e}_z), \quad (2)$$

where  $\vec{u}$  is the velocity field,  $\omega$  is the vorticity field, and  $\vec{e}_z$  is the unit vector in the direction of  $z$ -direction. All the variables are made dimensionless by means of the characteristic quantities. The cylinder radius  $a$  is used as the length scale while  $a/U$  is used as the time scale. The Reynolds number  $Re = 2Ua/\nu$  is based on the cylinder diameter  $2a$  and the magnitude  $U$  of the rectilinear velocity.

A non-rotating reference frame, translating with the cylinder is employed. In this frame the dimensionless boundary conditions for the problem of a rotating cylinder (with a time-dependent angular velocity  $\Omega(t)\vec{e}_z$ ) can be written as

$$\vec{u} = -\alpha(t)y\vec{e}_x + \alpha(t)x\vec{e}_y \quad \text{for } (x, y) \in \Gamma \quad (3)$$

and

$$\vec{u} = \vec{e}_x \quad \text{for } \sqrt{x^2 + y^2} \rightarrow \infty, \quad (4)$$

where  $\Gamma$  denotes the impermeable solid boundary of the cylinder. The angular/rectilinear speed ratio  $\alpha(t) = \Omega(t)a/U$  is the primary control parameter throughout this work.

In many practical numerical simulations for the laminar motion of viscous incompressible fluid, both the exterior and interior flow problems, the formulation based on velocity/vorticity variables would provide some advantages over the primitive-variable formulation. This velocity/vorticity formulation is especially well suited to treating initial development of the flow generated by impulsively started bodies, in which a relatively small vortical viscous region is embedded in a much larger inviscid potential flow. Consequently, the computational domain may be restricted to a smaller region where all vorticity contributions are contained.



Furthermore, the decoupling of the overall problem into its kinematic and kinetic aspects of the flow field gives an additional convenience. Throughout this work the vorticity transport equation described above may be viewed as kinetic process of the flow field in which the distribution of vorticity is interplayed by the process of convection, as well as the effects of viscous diffusion.

## 2.2 Integral Representation for Flow Kinematics

Having defined the governing equations for the rotating cylinder problem described above, we can now examine several advantages of an integral formulation used in this work. In the formulation of exterior flow problems, it is well known that one of the main numerical difficulties is related to the proper imposition of a prescribed limit value at the far-field for the unbounded physical domain in which the flow takes place. It should be pointed out that in any numerical simulation one has to restrict the exterior infinite domain to be finite with an artificial boundary. However, the far-field boundary in (4) fails to represent the exact characteristics at the outer perimeter of the finite computational domain. Therefore, in many practical applications, instead of directly applying the far-field boundary condition (4) one often tries to avoid the difficulty by utilizing various asymptotic boundary conditions at large distance (e.g. the application of potential flow or Oseen expansion), while others introduce a mapping of the infinite domain onto the finite one by means of a suitable coordinate transformation.

The other difficulty encountered in the simulation of viscous flow is that of prescribing the appropriate non-velocity boundary conditions at the solid surface. In general, the prescribed pressure at the solid boundary is needed in the application of primitive-variable (pressure/velocity) formulation, while the boundary vorticity is required for the formulation based on the velocity/vorticity (or stream-function/vorticity) variables. In order to overcome these two difficulties, we pose the kinematic relation on the problem by introducing a general Biot-Savart induced law described below.

In the problem with a viscous fluid, if the velocity distribution of  $\vec{u}$  are given, then the vorticity field  $\vec{\omega}$  could be evaluated through the kinematic relation between  $\vec{u}$  and  $\vec{\omega}$  described by  $\vec{\omega} = \nabla \times \vec{u}$  and  $\nabla \cdot \vec{u} = 0$ . On the other hand, the vector Poisson equation

$$\nabla^2 \vec{u} = -\nabla \times \vec{\omega}, \quad (5)$$

obtained from the continuity equation and the definition of vorticity, can be used to determine the velocity field from a given vorticity field.

For a general viscous flow in a region  $D$  bounded by an inner boundary  $\Gamma$  and outer boundary  $\Gamma'$ , we can recast the kinematic part of the problem into an equivalent integral formulation

$$\begin{aligned} \vec{u}(\vec{r}_0, t) = & -\frac{1}{c} \int \int_D \frac{\vec{\omega}(\vec{r}, t) \times (\vec{r} - \vec{r}_0)}{|\vec{r} - \vec{r}_0|^d} dA \\ & -\frac{1}{c} \int_{\Gamma+\Gamma'} \frac{[\vec{u}_b(\vec{r}, t) \cdot \vec{n}](\vec{r} - \vec{r}_0) - [\vec{u}_b(\vec{r}, t) \times \vec{n}] \times (\vec{r} - \vec{r}_0)}{|\vec{r} - \vec{r}_0|^d} \end{aligned} \quad (6)$$

where

$$c = \begin{cases} 4\pi, & \text{for } d = 3 \\ 2\pi, & \text{for } d = 2. \end{cases} \quad (7)$$

In the above integral representation,  $\vec{u}_b$  is the boundary velocity,  $\vec{n}$  is the outward normal unit vector and  $d$  is the spatial dimension. The subscript "0" denotes the field point where the velocity field is evaluated.

By applying the no-penetration and no-slip conditions to the rotating cylinder problem considered in this study, in two dimensions equation (6) can be written in terms of the rectilinear velocity  $U\vec{e}_x$  and the angular velocity  $\Omega(t)\vec{e}_z$  of the solid body  $B$  which is known as the generalized Biot-Savart law of induced velocity:

$$\begin{aligned} \vec{u}(\vec{r}_0, t) = & -\frac{1}{2\pi} \int \int_D \frac{\vec{\omega}(\vec{r}, t) \times (\vec{r} - \vec{r}_0)}{|\vec{r} - \vec{r}_0|^2} dA \\ & -\frac{1}{2\pi} \int \int_B \frac{2\vec{\Omega}(\vec{r}, t) \times (\vec{r} - \vec{r}_0)}{|\vec{r} - \vec{r}_0|^2} dA + \vec{U}. \end{aligned} \quad (8)$$

For detailed discussions of the integral representation for viscous flows the reader is referred to [46, 45]. Equation (8) represents the kinematic relationship between the velocity and vorticity fields of an infinite domain which is expressed as an integral form. The first integral

represents the contribution of the vorticity field to the development of the velocity field over the region  $D$  occupied by the viscous fluid, while the second integral gives the contribution from the rotation of the solid body. Notice that both the no-penetration, the no-slip boundary conditions on the solid surface and the far-field boundary conditions are implicitly imposed within the integral (8). To be precise, if we let the calculated field point  $\vec{r}_0$  go to infinite in (8), the vorticity contribution will approach zero. Consequently, the boundary condition at infinity is satisfied exactly in this integral representation of the kinematic relation. This indicates that the difficulty resulting from the imposition of far-field condition is removed by an application of (8).

In numerical simulations, it has been reported that the imposed boundary conditions at a large distance from the body will significantly influence the accuracy of the overall numerical solution [10, 19]. It is therefore necessary to devise a technique to impose the appropriate condition at the outer boundary of the computational domain. The integral approach in (8) provides a useful method to accomplish this. To be precise, the integral representation (8) permits us to determine the velocity (point-by-point) explicitly if all vorticity values are known everywhere in the domain of interest. It will exhibit a more realistic behavior at the outer perimeter of computational domain than those asymptotic techniques employed by other formulations. Namely, if the computational domain is large enough to contain all of vorticity generated around the solid boundary prior to a certain time, then at this instant the velocity on the outer perimeter of computational domain can be evaluated directly by the numerical integration of (8) with all the known vorticity field in the domain.

Additionally, if we apply equation (8) to the points of  $\vec{r}_b$  on the solid boundary, then the integral formula becomes

$$\begin{aligned} \vec{u}(\vec{r}_b, t) = & -\frac{1}{2\pi} \int \int_D \frac{\vec{\omega}(\vec{r}, t) \times (\vec{r} - \vec{r}_b)}{|\vec{r} - \vec{r}_b|^2} dA \\ & -\frac{1}{2\pi} \int \int_B \frac{2\vec{\Omega}(\vec{r}, t) \times (\vec{r} - \vec{r}_b)}{|\vec{r} - \vec{r}_b|^2} dA + \vec{U}. \end{aligned} \quad (9)$$

The boundary vorticity values are contained in this integral. Hence, by using the prescribed

motions of body (i.e.  $U$  and  $\tilde{\Omega}(t)$ ) and all of the known vorticity field in the domain, the determination of vorticity values at grid points on the solid boundary can be achieved by the numerical integration of equation (9). However, many implementations of flow simulations make use of approximate formulae for the boundary vorticity, which may lead to excessive error and thereby destroying the accuracy of the solutions.

When we solve the velocity field in an infinite domain we need only to take the viscous region ( $\mathfrak{V} \neq 0$ ) into account, while contributions from the inviscid region vanishes ( $\mathfrak{V} = 0$ ). Hence, an application of this integral representation allows one to confine the computation to the viscous region corresponding to the non-negligible vorticity portion of the flow, in contrast to employing domain methods (i.e. the finite-difference and finite-element methods) in which both potential and viscous regions are needed in a simultaneous solution. This implies the computational domain can be significantly reduced and hence a smaller number of grid points are needed than those required by standard finite-difference and finite-element methods.

### 2.3 General Body-Fitted Coordinate

In order to accommodate problems with a time-dependent domain in the physical  $(x, y)$  space, the vorticity transport equation (1) and Poisson equation (2) can be recast in terms of the time-varying generalized body-fitted coordinate system  $(\xi, \eta)$  as

$$\begin{aligned} \omega_t = & \frac{x_t}{J}(\omega_\xi y_\eta - \omega_\eta y_\xi) - \frac{y_t}{J}(\omega_\xi x_\eta - \omega_\eta x_\xi) \\ & - \frac{1}{J} [y_\eta(u\omega)_\xi - y_\xi(u\omega)_\eta + x_\eta(v\omega)_\xi - x_\xi(v\omega)_\eta] \\ & + \frac{2}{ReJ^2}(\sigma\omega_{\xi\xi} - 2\beta\omega_{\xi\eta} + \gamma\omega_{\eta\eta}) + \frac{2}{Re}(P\omega_\xi + Q\omega_\eta), \end{aligned} \quad (10)$$

and

$$\begin{cases} \sigma u_{\xi\xi} - 2\beta u_{\xi\eta} + \gamma u_{\eta\eta} + J^2(Pu_\xi + Qu_\eta) = J(x_\eta\omega_\xi - x_\xi\omega_\eta), \\ \sigma v_{\xi\xi} - 2\beta v_{\xi\eta} + \gamma v_{\eta\eta} + J^2(Pv_\xi + Qv_\eta) = J(y_\eta\omega_\xi - y_\xi\omega_\eta), \end{cases} \quad (11)$$

where

$$\begin{cases} \sigma = x_\eta^2 + y_\eta^2, & \beta = x_\xi x_\eta + y_\xi y_\eta, & \gamma = x_\xi^2 + y_\xi^2, \\ P = \xi_{xx} + \xi_{yy}, & Q = \eta_{xx} + \eta_{yy}, & J = x_\xi y_\eta - x_\eta y_\xi. \end{cases} \quad (12)$$

Here  $J$  is the Jacobian of the coordinate mapping between the physical space  $(x, y)$  and the computational space  $(\xi, \eta)$ . All subscripts in (10)-(12) denote partial differentiation. Also,  $u$  and  $v$  denote as the velocity component in  $x$ - and  $y$ -direction, respectively. Notice that this coordinate transformation will introduce two additional time-dependent terms  $x_t$  and  $y_t$  when a time-dependent flow domain in the physical space is considered. However, one can calculate the solution in a fixed time-independent computational grid in this generalized coordinate system because of the inclusion of  $x_t$  and  $y_t$  in the governing equations. Therefore, even when a time-dependent domain is considered, the interpolation of boundary conditions and grid points employed in the physical space formulation is not necessary in this generalized coordinate system. Moreover, it is also convenient to distribute the grid points within the domain of interest if a complex flow geometry is encountered. In fact, such a distribution of grid points is particularly important for simulations in viscous flows, where the grid points clustering near the surface is necessary to resolve the large gradients which appeared in a thin region due to the viscous effect.

Because we wish to extend the results presented here to more general problems with time-dependent domains, the computer code was written under this general body-fitted coordinate formulation. However, in this work, the polar coordinate  $(r, \theta)$  is used for the study of an unsteady flow around a rotating cylinder and the flow domain considered here is time-independent since a reference frame translating with the cylinder is used. If a body of arbitrary shape other than circular cylinder is considered (e.g. a rotating elliptic cylinder or airfoil) then the domain of interest becomes a time-dependent feature even though the reference frame is translating with the body. This occurs because of the rotational motion of an asymmetric bodies with respect to a non-rotating reference frame.

## 2.4 Computational Procedure

The computational domain is discretized in the body-fitted coordinate system  $(\xi, \eta)$  by setting  $\xi_i = i\Delta\xi$ ,  $\eta_j = j\Delta\eta$ , and  $i = 1, \dots, M$ ,  $j = 1, \dots, N$ , where  $M$  and  $N$  denote the number of grid points in the  $\xi$ - and  $\eta$ -direction, respectively. The numerical approximation of

the vorticity at the grid point  $(\xi_i, \eta_j)$  and time  $t^n = n\Delta t$  is denoted by  $\omega_{i,j}^n = \omega^n(i\Delta\xi, j\Delta\eta)$ . The vorticity transport equation (10) is first discretized by a second order central difference in the radial direction and a pseudospectral transform method in the circumferential direction for all spatial derivatives. This semi-discretization form of equation (10), consisting of a system of ordinary differential equations in time can be written as

$$\frac{d\hat{\omega}}{dt} = F(\hat{\omega}), \quad \hat{\omega} = (\omega_{2,2}, \dots, \omega_{M-1,N-1})^T, \quad (13)$$

for all the interior grid points. Therefore, the calculation procedure to advance the solution for any given time increment can be summarized as follows:

*Step 1: Internal vorticity over the fluid region at each interior field point is calculated by solving the discretized vorticity transport equation. An explicit second-order rational Runge-Kutta marching scheme based on the work of [41] is used to advance in time for (13)*

The discretization of (13) in time thus can be written as

$$\hat{\omega}^{n+1} = \hat{\omega}^n + \frac{2\hat{g}_1(\hat{g}_1, \hat{g}_3) - \hat{g}_3(\hat{g}_1, \hat{g}_1)}{(\hat{g}_3, \hat{g}_3)}, \quad (14)$$

with

$$\begin{cases} \hat{g}_1 = F(\hat{\omega}^n)\Delta t \\ \hat{g}_2 = F(\hat{\omega}^n + c\hat{g}_1)\Delta t \\ \hat{g}_3 = (1-b)\hat{g}_1 - b\hat{g}_2 \end{cases} \quad (15)$$

where  $(\cdot, \cdot)$  denotes the scalar product. In order to ensure the stability of the above nonlinear explicit scheme, the two constants  $b$  and  $c$  in (15) must satisfy  $bc = -0.5$ . In particular,  $b = -1$  and  $c = 0.5$  are used in our computations. Although this method is explicit in nature, it may become unconditionally stable by the suitable choice of the constants in (15) [17]. In addition, this particular scheme allows one to use a larger time-step than that of the three-step Adams-Bashforth scheme used by Chen [5]. This step consists of the kinetic part of the computational loop.

*Step 2: Using known internal vorticity values at all the interior grid points from step 1, the generalized Biot-Savart law of induced velocity (9) is used to update the boundary vorticity values at all the surface nodes.*

*Step 3: At this stage, all the vorticity values in the computational domain are known at the new time level. Then, the velocity at points on the outer perimeter of the computational domain is calculated by the integral kinematic constraint (8).*

Notice that at each time step, the numerical integration of the first integral over the fluid region in (8) is carried out by means of an isoparametric formulation which is used extensively in the finite element method, while the second integral can be evaluated analytically over the solid body  $B$ . The vorticity distribution over each distorted quadrilateral element in the physical space are actually performed over a square in the isoparametric space. Further details of the integration method can be found in Chen [5].

It is worthy of note that the evaluation of the integral (8) involves a problem associated with the non-uniqueness of the solution. The principle of vorticity conservation imposed by Wu [45] resolve such difficulty. For flows past single or multiple solid bodies, a more immediate improvement to the principle of vorticity conservation is provided by Chen [5].

*Step 4: The new internal velocity field can be established by solving the Poisson equations (11) with prescribed solid boundary conditions and outer boundary conditions of the velocity that have been determined from step 3.*

The final form of the discretized Poisson equations can be written

$$\begin{cases} \mathbf{A}\mathbf{u} = \mathbf{f}_1 \\ \mathbf{A}\mathbf{v} = \mathbf{f}_2, \end{cases} \quad (16)$$

where  $\mathbf{u}$  and  $\mathbf{v}$  are two vectors of unknown interior nodal values. Also,  $\mathbf{A}$  is a 11-banded matrix, while  $\mathbf{f}_1$  and  $\mathbf{f}_2$  are vectors associated with the known forcing terms and boundary conditions. The resulting 11-banded matrix equations are then solved by a preconditioned biconjugate gradient routine [6]. This step completes the computational loop for each time level.

One further important point to be noted in the integral approach is that the initial flow field can be determined by the same solution procedure described above (from step 2 to step 4). To be more precise, at time  $t = 0^+$  the unknown boundary vorticity values is determined by solving integral (9) with zero vorticity values everywhere away from the solid

boundary surface. This is based on the fact that the vorticity will concentrate on the body surface in the form of a vortex sheet immediately after the body impulsively started. This approach therefore reduces equation (9) to a boundary integral, indicate that the method can be viewed as the boundary element method utilized in the problem of the potential flow. Once the boundary vorticity values are obtained, the initial velocity field can be determined by solving equation (11) with the known velocity values at all points on the outer perimeter of the computational domain which have been calculated by the integral (8). In contrast to the special technique used by other methods, this integral approach enables the numerical code to generate the initial velocity field simply by the implementation of one cycle of a solution procedure rather than employing any additional treatments.

### 3. RESULTS AND DISCUSSIONS

In this section we apply the numerical scheme described above to simulate and control the unsteady flow around a rotating cylinder that undergoes a variety of steady and unsteady angular/rectilinear speed ratios at a Reynolds number of 200. The choice of this particular Reynolds number is not due to the limitation of the numerical algorithm, it is mainly for the purpose of comparing with the existing experiments of Coutanceau and M  nard in the case of constant rotation for a rotating cylinder [8]. In this model, the rectilinear velocity is fixed as a constant value while the angular velocity is treated as a control variable.

Although the choice of time-dependent rotation rates that may be used to control the rotating cylinder are unlimited, the computational results presented here are restricted to the following three types of rotation:

1. Constant speed of rotation:  $\alpha(t) = \text{constant}$ .
2. Time-harmonic rotary oscillation:  $\alpha(t) = A \sin \pi F t$ .
3. Time-periodic rotation:  $\alpha(t) = A |\sin \pi (F/2) t|$ .

Again, this choice was made because it allowed us to compare experimental and numerical results and it matched the control experiments of Modi [25, 24]. All variables are normalized



to the nondimensional forms in the formulation. In a non-rotating frame attached to the cylinder, the configurations for the different controls considered in the physical space are sketched in Figure 1, together with the corresponding time evolution of the angular velocity.

Concerning the use of a time-harmonic rotary oscillation, it is common to define the motion of angular rotation  $\Theta(t)$  as

$$\Theta(t) = -\theta \cos 2\pi f t, \quad (17)$$

where  $\theta$  is the angular amplitude and  $f$  is the forcing frequency of the oscillation. Thus, the associated time-dependent speed ratio is given by

$$\alpha(t) = \frac{a\Omega(t)}{U} = A \sin \pi F t, \quad (18)$$

where  $F = 2af/U$  is the reduced forcing frequency and  $A = \pi F\theta$  is the normalized maximum rotation rate of the forcing oscillation. In order to attain high lift and reduced drag, previous work for constant rotation rates [7] lead us to consider one special type of time-periodic rotation. That is, the cylinder under control is rotated in the counterclockwise direction about its axis with a time-periodic speed ratio given by

$$\alpha(t) = A |\sin \pi (F/2)t|. \quad (19)$$

Here, the reduced forcing frequency of this particular time-periodic rotation is  $F$ . This particular type of rotation is expected to provide a substantial lift enhancement and drag reduction through a proper choice of both the angular amplitude (thus the normalized maximum rotation rate  $A$ ) and forcing frequency (thus the reduced frequency  $F$ ). This improvement can be demonstrated by comparing its respective force performances against the time-harmonic rotary oscillation.

The major goal of this paper is to study the effect of rotation rate control upon the lift and drag on the cylinder surface. Hence, in the following discussion we concentrate on various issues concerning the development of temporal forces. In a viscous flow, it is well known that the total lift and drag forces are contributed by the pressure and skin friction due

to the viscous effects. An important consequence of using the velocity/vorticity formulation is that the forces can be directly evaluated from the known vorticity on the cylinder surface. Hence, for known vorticity values on the cylinder surface, the lift and drag coefficients can be calculated in the  $r$ - $\theta$  coordinates by

$$C_L(t) = C_{Lp}(t) + C_{Lf}(t) = -\frac{2}{Re} \int_0^{2\pi} \left( \frac{\partial \omega(t)}{\partial r} \right)_\Gamma \cos \theta d\theta + \frac{2}{Re} \int_0^{2\pi} \omega(t)_\Gamma \cos \theta d\theta, \quad (20)$$

and

$$C_D(t) = C_{Dp}(t) + C_{Df}(t) = \frac{2}{Re} \int_0^{2\pi} \left( \frac{\partial \omega(t)}{\partial r} \right)_\Gamma \sin \theta d\theta - \frac{2}{Re} \int_0^{2\pi} \omega(t)_\Gamma \sin \theta d\theta, \quad (21)$$

where the subscript  $\Gamma$  denotes quantities evaluated on the cylinder surface. The subscripts  $p$  and  $f$  represent the contribution from pressure and skin friction, respectively. In particular, we denote the positive values of  $C_L$  in the negative  $y$ -direction (as noted in Figure 1).

To assess the accuracy of the numerical algorithm, computations were first performed over a wide range of constant speed ratios up to 3.25 at a Reynolds number of 200. Several particular speed ratio parameters were chosen to allow for the comparison against the experimental work of Coutanceau and M  nard [8]. Speed ratios greater than 2 are important in the study of the possibility of suppressing vortex shedding by an application of higher rotation rates. The details of the work using constant rotation rates were reported in [7], where several numerical solutions were compared and demonstrated to be in good agreement with experimental results.

In the computations below, a fixed flow domain is used and its extent is essentially determined by the time-span under investigation. Namely, a larger computational domain will be needed for a longer time of observation. Here, a circle of radius  $r = 24$  and  $r = 36$  are chosen for the time-span of  $0 \leq t \leq 24$  and  $0 \leq t \leq 36$ , respectively. These long time histories were necessary to demonstrate the periodicity of the flow pattern and evolution of the forces. When a larger domain is considered, the mesh is increased in the radial direction in order to properly discretize the domain. A uniformly spaced  $M = 128$  in circumferential direction is used for all computations, while  $N = 120$  and  $N = 180$  stretched grid lines

in the radial direction are used for the time-span under consideration. In the numerical calculations, small initial time steps are taken in order to contain the inherent numerical error caused by resolving of the infinitesimal vorticity layer at  $t = 0^+$ . A detailed discussion of the algorithm and the accuracy of the initial flow field can be found in [7].

### 3.1 Constant Speed of Rotation

Figures 2(a,b) show calculated instantaneous streamline plots for a constant value of speed ratio of  $\alpha = 2.07$  at  $Re = 200$  and compare these plots with the experimental work of Coutanceau and M  nard [8]. In the computation, the non-rotating reference frame is translating with the cylinder while the camera in the experiment is moving with the cylinder as well. Excellent agreement is obtained, despite the fact that a high velocity gradient is induced in the near wake due to the cylinder rotation. Although not shown here, one particular interesting feature is the difference between the experimental work and our calculated observation regarding the conclusion of suppressing of vortex shedding at high speed ratios. In the computation using high speed ratios (at  $Re = 200$ , as reported in [7]), the calculated equi-vorticity contours seem to imply that vortex shedding continues to occur even at high rotation rates ( $\alpha \geq 2.07$ ). However, at these high  $\alpha$ , the observed formation of the vortex street behind a rotating cylinder seems to contradict the experimental conclusion described in [8]. This difference is due to the fact that the experimental apparatus was such that only 10 dimensionless time units of data could be collected and in part by the flow visualization techniques used in their experiments. On the other hand, it is important to note a recent investigation by Badr et al. [2] regarding the issue of suppressing of vortex shedding. Their tests were performed both experimentally and numerically at Reynolds numbers of  $Re = 10^3$  and  $Re = 10^4$ . For a rotation rate of  $\alpha = 3$  at  $Re = 10^3$ , they show that no other eddy is created after the shedding of two vortices. In addition, the temporal evolutions of the lift and drag coefficients imply that a steady state is indeed approached.

Figure 3 shows plots of the time histories of lift, drag and lift/drag coefficients at various values of speed ratios ( $0 < \alpha \leq 3.25$ ) and for time in the interval  $0 \leq t \leq 24$ . As seen in Fig-

ure 3(a), when the speed ratio is increased to 2.07, the lift increases timewise proportionally. However, as the speed ratio further increases, lift appears to initially decrease then increases gradually at later times. Not surprisingly, the maximum value of  $C_L$  that can be achieved by rotation is also higher as the speed ratio grows. It is also observed that, at speed ratios lower than 2, the respective lift curves exhibit a well established periodic evolution. However, in the range of  $\alpha > 2$ , it is not known whether the nature of this periodicity will continue if the time of investigation is expanded. Apparently, as can be seen from Figure 3(a), the cylinder rotation (as a boundary moving mechanism) does yield a substantial lift enhancement as indicated by the experimental work of Modi's group for airfoil/rotating cylinders configurations.

As illustrated by the drag curve in Figure 3(b), there is a substantial increase in drag when the speed ratio is increased. In all cases considered here, these drag curves seem to converge after a certain time and then oscillate under different amplitudes and frequencies thereafter. Detailed numerical results on the effect of the speed ratio to the resulting lift/drag curve are shown in Figure 3(c). In the range  $0 < \alpha < 2.07$ , the lift/drag performance appears to improve timewise (for  $0 < t \leq 24$ ) with an increase of  $\alpha$ . If a comparison is made between  $\alpha = 2.07$  and  $\alpha = 0.05$ , a noticeable improvement of the lift/drag performance is observed. Although a higher lift/drag ratio is achieved by increasing the rotation rate in this range, the question arises whether any further increase of  $\alpha$  will result in a continued improvement of the lift/drag ratio. Intuitively, it is natural to expect a monotonical increase in the lift/drag ratio as  $\alpha$  increases to  $\alpha = 3.25$ . However, this is not the case as a comparison is made between  $\alpha = 3.25$  and  $\alpha = 2.07$ . In fact, the lift/drag curves illustrate a gradual decrease in performance over certain time interval when the speed ratio increases beyond 2. Moreover, this tendency toward lower lift/drag ratio becomes noticeable when  $\alpha$  reaches the highest value ( $\alpha = 3.25$ ) considered here. Nevertheless, for all  $\alpha$  considered here, a significant increase in the maximum value of  $C_L/C_D$  can be obtained by increasing  $\alpha$ . However, it is found that it will reach its maximum value at a much later time for higher values of  $\alpha$ .

### 3.2 Time-Periodic Rotation vs. Time-Harmonic Rotary Oscillation

The previous results only applied to constant rotation rates. In this section we consider time-varying rotations. Although the maximum value of lift/drag ratio can be achieved at a certain optimal constant rotation rate described above, this does not immediately imply that the constant rotation will always yield a global maximum value of the lift/drag ratio over a specific time interval. In fact, the general problem is to determine the optimal control input among all time dependent rotation rates. As a first step towards solving this problem, one needs to extend the computational calculations to the case of arbitrary time-dependent rotation rates. Since we shall not attempt to solve the necessary conditions corresponding to the optimal rotation rate problem and because the main goal of the paper is to gain insight into the possible form of an optimal controller, we shall concentrate on two periodic inputs and investigate the impact of each control on this problem. Hence, to keep the paper of reasonable length and the simulations simple we restrict our study to two periodic inputs.

It is well known that when a cylinder oscillates in a uniform flow, the associated forcing oscillating frequency and amplitude can influence the vortex formulation and forces response substantially [42, 44]. It has been experimentally shown that at  $Re = 200$ , the natural Strouhal frequency of a non-rotating circular cylinder ( $\alpha = 0$ ) is approximately  $F_n = 0.185$  [43]. It is of important to study the behavior of fluctuating forces at imposed forcing frequencies which lie in the neighborhood of the natural frequency. The temporal evolutions of lift, drag and lift/drag are shown separately in Figures 4(a,b,c) for a time-periodic rotation  $\alpha(t) = |\sin 0.25t|$  and a time-harmonic rotary oscillation  $\alpha(t) = \sin 0.5t$ , respectively. In the case of time-periodic rotation, the cylinder under control is rotated in the counterclockwise direction about its axis with a time-periodic angular velocity. Notice that these two types of rotation are employed by the same forcing frequency (i.e.  $F = 0.16$ ) which lies in the neighborhood of the natural frequency. The numerical results clearly confirm the expected benefit of this time-periodic rotation for both lift and drag forces, as shown in Figure 4.

In comparing these two types of rotation, it should be noted that rotating in the same

direction causes the lift curve to be shifted upwards due to the nature of rotation, while the drag curve is shifted downwards. In terms of performance, this corresponds to an increase of the time-averaged lift force in the time-span of the investigation, while in the same time interval, a substantial reduction of the time-averaged drag as well. The resulting improvement of the lift/drag ratio is shown in Figure 4(c).

To demonstrate the influence of this time-periodic rotation on the temporal development of these force coefficients, two additional values of the forcing frequency were tested. In Figure 5, all the time histories of lift, drag and lift/drag coefficients are shown for a forcing frequency (i.e.  $F = 0.08$ ) which is  $1/2$  the frequency in Figure 4. As it can be seen from Figure 5(a), except in an initial stage, lift is increased for the time-periodic rotation ( $\alpha(t) = |\sin 0.125t|$ ) when compared to the time-harmonic rotary oscillation ( $\alpha(t) = \sin 0.25t$ ). Also the drag is reduced as illustrated in Figure 5(b). However, the amount of drag reduction is not significant over the time-span of the investigation. As would be expected, the resulting lift/drag curves shown in Figure 5(c) exhibit almost the same behavior as those lift curves illustrated in Figure 5(a).

Similar results are shown in Figure 6, where a higher rotation frequency (i.e.  $F = 0.32$ ) is imparted to the cylinder. As before, the time-periodic rotation at this frequency enhances the lift performance when compared to the time-harmonic rotary oscillation. However, notice that the corresponding drag curves are oscillating about an "average value" in the time interval under consideration, for both types of rotation. The improvement in the lift/drag curve shown in Figure 6(c) is more noticeable when compared to the lift/drag curve in Figure 4(c). Notice that none of the frequencies considered in Figures 5 and 6 are in the neighborhood of the natural frequency.

In a detailed examination of all comparisons between two types of rotations mentioned above, it is found that lift enhancement is not always timewise in the time interval under investigation. The exact time at which the time-periodic rotation outperform the time-harmonic rotary oscillation depends on the forcing frequency imparted to the cylinder. This

occurs earlier for a higher value of forcing frequency. However, the drag curves have a significantly different character. The decrease or increase in drag depends on whether its forcing frequency lies in the neighborhood of natural frequency or not. If the forcing frequency is in the neighborhood of the natural frequency as the case in Figure 4(b), the drag curve exhibits a substantial reduction. On the other hand, for the forcing frequencies which are not in the neighborhood of the natural frequency as shown in Figures 5(b) and 6(b), the drag curves changes only slightly. In addition, for these forcing frequencies, the respective lift/drag curves are similar to the corresponding lift curves. This is due to the minor variations in the drag curves.

### 3.3 Effects of Forcing Frequency and Angular Amplitude

Because of the above observations, it is worthwhile to investigate the effects of various control parameters upon the force coefficients. A comparisons of force coefficients are shown in Figure 7, corresponding to all three forcing frequencies described above. It can be readily seen that these forcing frequencies have considerable influence on the amplitude and frequency of the oscillatory forces.

In terms of performance, Figure 7(a) presents the evolution of lift coefficients and shows no clear advantage of changing the forcing frequency. However, as shown in Figures 7(a,b), the rotation ( $\alpha(t) = |\sin 0.25t|$ ) which lies in the neighborhood of the nature frequency achieves a higher value of  $(C_L)_{max}$ , and yields a slightly larger value of drag when compared to the other two cases (namely,  $\alpha(t) = |\sin 0.125t|$  and  $\alpha(t) = |\sin 0.5t|$ ). The lift/drag curves shown in Figure 7(c) exhibit similar temporal evolutions.

It is also interesting to study the effect of angular amplitude on the temporal evolution of forces while the forcing frequency is fixed as a constant. Figure 8 shows that resulting forces on the cylinder can differ significantly at different angular amplitudes for  $\alpha(t) = A|\sin 0.314t|$ . This rotation corresponds to a forcing Strouhal number of 0.2 which is in the neighborhood of the natural Strouhal number of 0.185. The angular amplitudes considered were  $A = 1.0, 2.07$  and  $3.25$ . Apparently, as can be seen from these figures, a larger angular

amplitude definitely yields an incremental lift coefficient over the time-span of investigation ( $0 \leq t \leq 36$ ). However, initially the drag increases with an increase of  $A$ , then after a certain time it oscillates with almost the same amplitude and frequency around an averaged value. Consequently, this leads to a substantial improvement in lift/drag with increasing  $A$ , as clearly shown in Figure 8(c). Nevertheless, the effect of angular amplitude is very noticeable when compared to the effect of the forcing frequency shown in Figure 7.

### 3.4 Time-Averaged Value of Forces

We also examined the averaged values of the force coefficients over the time span of investigation as various control parameters are altered. The time-harmonic rotary oscillation ( $\alpha(t) = \sin \pi F t$ ) described in §3.2 was considered with three different values of forcing frequency. The forces were averaged with respect to the time ( $0 \leq t \leq 24$ ). Figure 9(a) shows the time-averaged values of lift, drag, lift/drag as the forcing frequency  $F$  is varied between 0.08 and 0.32. This figure shows that the forcing frequency has a considerable influence on the time-averaged values of the force coefficients. The local maximum values of time-averaged lift, drag and lift/drag ratios correspond to the forcing frequency which lies in the neighborhood of the natural frequency. This particular feature was also observed in the numerical results of Mo [23] where it was shown that the drag peak occurs at the forcing frequency equal to the natural frequency.

As for the cases of time-periodic rotation, variations of time-averaged forces coefficients with respect to the forcing frequency are presented in Figure 9(b). As illustrated in the figure, a forcing frequency in this range (i.e.  $0.08 \leq F \leq 0.32$ ) has little effect on the time-averaged forces. Although the difference in time-averaged drag is minor, the forcing frequency which lies in the neighborhood of the natural frequency ( $F = 0.185$ ) corresponds to a larger time-averaged drag and a smaller time-averaged lift.

The effect of angular amplitude on the time-averaged values of lift, drag and lift/drag coefficients is shown in Figure 9(c), for  $\alpha(t) = A|\sin 0.314t|$  averaged over  $0 \leq t \leq 36$ . For  $A$  in the range,  $1 \leq A \leq 3.25$ , all the time-averaged values are almost linearly proportional



to the angular amplitude. Significant increases in lift coefficients with increasing angular amplitude is particularly noticeable. This can be demonstrated by comparing the case  $A = 3.25$  with  $A = 1$ . It represents a 240% increment of lift performance. However, a slight increment in the drag coefficients with increasing angular amplitude is also observed. A moderate improvement of time-averaged lift/drag ratio is also seen.

In the case of a constant speed of rotation, it is also worthwhile to study the effect of speed ratios on the time-averaged lift, drag and lift/drag coefficients. These results are shown in Figure 10(a) for  $\alpha$  in the range,  $0 < \alpha \leq 3.25$ , and in the time interval  $0 < t \leq 24$ . It illustrates that the time-averaged lift is almost linearly proportional to the speed ratio, while the time-averaged drag remains as a constant value up to  $\alpha = 2$ , then monotonically increases with speed ratio thereafter. Most importantly, the time-averaged lift/drag is *not* linearly proportional to the speed ratio. As shown in the figure, the highest value of the speed ratio  $\alpha = 3.25$  considered here is not the optimal constant rotation rate corresponding to the maximum value of time-averaged lift/drag. The maximum value occurs at a lower speed ratio, approximately  $\alpha = 2.38$ , and it represents a substantial increase of 440% over the lower speed ratio  $\alpha = 0.5$ . In Figure 10(b), the variation of the (total lift)/(total drag) force ratio with respect to the speed ratio is shown for  $\alpha$  in the range  $0 < \alpha \leq 3.25$ . Although a maximum is achieved at a value between  $\alpha = 2.0$  and  $\alpha = 2.38$ , it should be noted that this optimal speed ratio is not necessarily the same optimal value as described in Figure 10(a).

The results presented in Figures 10(a,b) demonstrate an effective way of improving lift/drag performance by changing the rotation rate and illustrate the importance of selecting a proper rotation rate in order to maximize performance. If one formulates this problem as an optimal control problem, then the time-averaged lift/drag ratio in Figure 10(a) represents the cost function and the goal is to find an optimal control  $\alpha_1^*$ , among a set of restricted control parameters (constant values), that will provide the maximum value of the time-averaged

performance functional

$$J_1(\alpha) = \frac{1}{T_f} \int_0^{T_f} \left[ \frac{C_L(t, \alpha)}{C_D(t, \alpha)} \right] dt, \quad (22)$$

where  $T_f$  is the final time. Similarly, the curve in Figure 10(b) represents the optimal control problem defined by maximizing the cost functional

$$J_2(\alpha) = \frac{\int_0^{T_f} C_L(t, \alpha) dt}{\int_0^{T_f} C_D(t, \alpha) dt}. \quad (23)$$

In theory, these optimal control problems can be solved by applying necessary conditions for distributed parameter systems. However, computational methods for such necessary conditions are complex and not yet fully developed. The results presented here may be used to guide and test future computational schemes based on optimal control theory.

### 3.5 Synchronizations of Cylinder and Wake

The synchronization of cylinder and wake has long been known to be an important component of vortex-induced oscillations [33]. A detailed study of various types synchronization for a body oscillating transversely in a uniform stream can be found in Williamson and Roshko [44]. For the case of time-periodic rotation considered here, it is natural to ask whether such synchronization can occur and how well the numerical results can predict the occurrence of this important phenomenon. To the best of our knowledge, the current study is the first work to investigate synchronization under the particular form of time-periodic rotation described in previous sections.

An examination of the responses in Figure 4, shows that the combined system of cylinder and wake will be “locked in” by an imposed forcing frequency. This synchronization of the cylinder and wake is due to the fact that the forcing frequency of rotation ( $F = 0.16$ ) lies in the neighborhood of the natural frequency ( $F_n = 0.185$ ). Notice that in the case of time-periodic rotation shown in Figure 4, both lift and drag curves oscillate with the forcing frequency (corresponding to a time period of  $T = 12.5$ ), clearly exhibiting a periodic response. However, in the case of time-harmonic rotary oscillation, the lift curve oscillates

with the same forcing frequency ( $T = 12.5$ ) while drag curve oscillates with the period of  $T/2$ . Consequently, the lift/drag ratios oscillate at the same frequency ( $T = 12.5$ ) for both types of rotation.

For the case of time-periodic rotation  $\alpha(t) = A|\sin 0.314t|$ , we extend our observation to a relatively longer time. For  $0 < t \leq 36$ , an examination of these force curves for  $A = 1.0$  in Figure 8 exhibits a periodic response with a frequency ( $F = 0.2$ ) precisely equal to the input forcing frequency (i.e.  $T = 10$ ). Although this periodic behavior is not established for  $A = 2.07$  and  $3.25$ , the corresponding curves are almost periodic in time. In order to confirm this periodicity, a sequence of instantaneous streamlines are shown in Figure 11. In Figure 11, each plot is separated with an interval of one time period. These streamlines are plotted in a frame fixed with the undisturbed fluid. The periodicity of the flow is clearly noticeable. Two opposite-sign vortices are shed alternately on opposite sides of the cylinder at each cycle of rotation. The vortex formation in the wake is similar to the case of a non-rotating cylinder ( $\alpha = 0$ ). However, the midline of the vortex street has been displaced slightly upwards due to the nature of rotation (in the counterclockwise direction).

In order to identify the range of frequency for this fundamental synchronization, we impose a rotation rate  $\alpha(t) = |\sin 0.283t|$  with a forcing frequency ( $F = 0.18$ ) which is the neighborhood of the natural frequency. The time histories of lift, drag and lift/drag coefficients shown in Figures 12(a,b,c) clearly demonstrate the periodic behavior of the response. The corresponding streamline plots (at each instant) are presented in Figure 13. These results show that there exists a range of forcing frequencies in which fundamental synchronization will occur. However, the precise range of forcing frequencies leading to synchronization has not yet been determined (computational time is the limiting factor).

In the case of time-harmonic rotary oscillation, the effects of the forcing frequency and amplitude on a cylinder wake have been investigated experimentally by Tokumaru and Dimotakis [40]. Several vortex formations were observed in the wake. Their experiments dealt with a range of amplitudes and frequencies at a Reynolds number of  $Re = 1.5 \times 10^4$ . By fixing

the reduced amplitude  $A$  in their experiments, four qualitatively different vortex shedding modes were identified when the forcing frequency was increased. Although their experiments were conducted at a Reynolds number higher than the current study ( $Re = 200$ ), we conducted a similar investigation. Here, a particular value of the rotation rate  $\alpha(t) = 2 \sin 3.14t$  (corresponding to  $A = 2$  and  $F = 1.0$ ) was tested. Figure 14 shows the lift and drag histories up to  $t = 36$ . These curves are clearly periodic in nature. Under this forcing frequency, the lift curve oscillates with a period of  $T = 10$ , while the drag curve oscillates with a period of  $T = 5$ . The instantaneous streamlines plots are presented in Figure 15, and they show a time periodic flow pattern. Moreover, these results indicate that rotation may provide an effective control of the cylinder wake.

#### 4. CONCLUSIONS

An algorithm for computing the viscous flow past a rotating cylinder is presented and applied to the problem of controlling cylinder forces by rotation. Several fundamental types of rotation were considered. Using time-periodic rotations leads to a considerable improvement in the force coefficients and was shown to be very effective, especially compared to time-harmonic rotary oscillations. These results are significant because they show a proper choice of the rotation rate can lead to improved flow fields. Very precise periodicity of the force for certain cases was established, and this periodic behavior has considerable impact on controlling the vortex formation in the cylinder wake. For the case of a constant speed of rotation, two optimal control problems were considered and solved computationally.

These results demonstrate the feasibility of using boundary mechanisms for controlling unsteady flows, and consequently can be applied to enhance the performance. Using such mechanisms as a controller allows us to formulate a wide variety of optimal control problems for fluid flow systems. Modifications of existing numerical algorithms needed for such control problems depend on performance and design constraints. For example, one may need the maximum (or minimum) lift to drag ratio in order to sustain a particular maneuver of a supermaneuverable aircraft. Because of the complexity and importance of the relationship

between vortex motion and cylinder forces, the first step in control design may be to seek a specific type of rotation rate that will match all proposed goals.

A precise understanding of time-dependent moving surfaces in boundary layer control may provide an effective way for lift enhancement and drag reduction. By treating the rotation rate as a control variable in this model, we will eventually be interested in finding the optimal control (i.e. a time history of the rotation rate) that maximizes (or minimum) the lift-to-drag ratio over a fixed time interval. Although here the optimal control problem associated with the constant rotation rate was solved by direct computations, it is still important to explore the possible implementation of a computational algorithm to calculate the optimal solution for the more general problems. The tools developed here can be used to investigate fundamental questions regarding control of separated flows by using various boundary control mechanisms. Future work needs to be done in the development of new computational algorithms for solving complex optimal flow control problems.

## References

- [1] F. Abergel and R. Temam. On some control problems in fluid mechanics. *Theoret. Comput. Fluid Dynamics*, 1:303–325, 1990.
- [2] H. M. Badr, M. Coutanceau, S. C. R. Dennis, and C. Ménard. Unsteady flow past a rotating circular cylinder at Reynolds numbers  $10^3$  and  $10^4$ . *J. Fluid Mech.*, 220:459–484, 1990.
- [3] H. M. Badr and S. C. R. Dennis. Time-dependent viscous flow past an impulsively started rotating and translating circular cylinder. *J. Fluid Mech.*, 158:447–488, 1985.
- [4] J. A. Burns and S. Kang. A control problem for burgers' equation with bounded input/output. *Nonlinear Dynamics*, 2:235–262, 1991.
- [5] Y.-M. Chen. *Numerical simulation of the unsteady two-dimensional flow in a time-dependent doubly-connected domain*. PhD thesis, University of Arizona, 1989.

- [6] Y.-M. Chen, A. E. Koniges, and D. V. Anderson. ILUBCG2-11: Solution of 11-banded nonsymmetric linear equation systems by a preconditioned biconjugate gradient routine. *Comp. Phys. Comm.*, 55:359–365, 1989.
- [7] Y.-M. Chen, Y.-R. Ou, and A. J. Pearlstein. Development of the wake behind a circular cylinder impulsively started into rotatory and rectilinear motion: intermediate rotation rates. ICASE Report 91-10, *J. Fluid Mech.*, in the press, 1993.
- [8] M. Coutanceau and C. M  nard. Influence of rotation on the near-wake development behind an impulsively started circular cylinder. *J. Fluid Mech.*, 158:399–446, 1985.
- [9] H. Fattorini and S. S. Sritharan. Existence of optimal controls for viscous flow problems. *Proc. R. Soc. Lond. A*, 439:81–102, 1992.
- [10] B. Fornberg. A numerical study of steady viscous flow past a circular cylinder. *J. Fluid Mech.*, 98:819–855, 1980.
- [11] M. Gad-el-Hak. Flow control. *Appl. Mech. Rev.*, 42:261–293, 1989.
- [12] M. Gad-el-Hak and D. M. Bushnell. Separation control: Review. *J. Fluid Engrg*, 113:5–30, 1991.
- [13] R. Glowinski. Finite elements for the numerical simulation of incompressible viscous flow. Introduction to the control of the Navier-Stokes equations. Research Report UH/MD-94, University of Houston,.1990.
- [14] M. D. Gunzburger, L. S. Hou, and T. P. Svobodny. Numerical approximation of an optimal control problem associated with the Navier-Stokes equations. *Appl. Math. Lett.*, 2:29–31, 1989.
- [15] M. D. Gunzburger, L. S. Hou, and T. P. Svobodny. Analysis and finite element approximation of optimal control problems for stationary Navier-Stokes equations with distributed and neuman controls. *Mathematics of Computations*, 57:123–151, 1991.

- [16] M. D. Gunzburger, L. S. Hou, and T. P. Svobodny. Boundary velocity control of incompressible flow with an application to drag reduction. *SIAM J. Control and Optim.*, 30:167-181, 1992.
- [17] E. Hairer. Unconditionally stable explicit methods for parabolic equations. *Numerische Mathematik*, 35:57-68, 1980.
- [18] W. B. Herbst. Supermaneuverability. In Francis & Luttges, editor, *Workshop on Unsteady Separated Flow*. Sponsored by AFOSR, FJSRL, U. of Colorado, 1983.
- [19] D. B. Ingham. Steady flow past a rotating cylinder. *Computers & Fluids*, 11:351-366, 1983.
- [20] K. Ito and S. Kang. A dissipative feedback control synthesis for systems arising in fluids dynamics. Submitted to *SIAM J. Control and Optim.*, 1992.
- [21] Antony Jameson. Automatic design of transonic airfoil to reduce the shock induced pressure drag. In *the 31st Israel Annual Conference on Aviation and Aeronautics*, Feb. 1990.
- [22] C. A. Koromilas and D. P. Telionis. Unsteady laminar separation: an experimental study. *J. Fluid Mech.*, 97:347-384, 1980.
- [23] J. Mo. *An investigation on the wake of a cylinder with rotational oscillations*. PhD thesis, U. of Tennessee Space Institute, 1989.
- [24] V. J. Modi, F. Mokhtarian, M. Fernando, and T. Yokomizo. Moving surface boundary-layer control as applied to two-dimensional airfoils. *J. Aircraft*, 28:104-112, 1991.
- [25] V. J. Modi, F. Mokhtarian, and T. Yokomizo. Effect of moving surfaces on the airfoil boundary-layer control. *J. Aircraft*, 27:42-50, 1990.

- [26] Y.-R. Ou. Control of oscillatory forces on a circular cylinder by rotation. In *4th. International Symposium on Computational Fluid Dynamics*. U. of California, Davis, September 1991.
- [27] Y.-R. Ou. Active flow control relative to a rotating cylinder. In *Proceedings of the 31st IEEE Conference on Decision and Control*, pages 3399–3404, Tucson, AZ., December 1992.
- [28] Y.-R. Ou and J. A. Burns. Optimal control of lift/drag ratios on a rotating cylinder. *Appl. Math. Letters*, 5:57–62, 1992.
- [29] D. S. Park, D. M. Ladd, and E. Hendricks. Feedback control of karman vortex shedding. In *Symposium on Active Control of Noise and Vibration*, Anaheim, California, November 1992. ASME Winter Annual Meeting.
- [30] L. Prandtl. Über flüssigkeitsbewegung bei sehr kleiner reibung. In *Proc. Third Int. Math. Congr.*, pages 484–491, Heidelberg, Germany, 1904.
- [31] L. Prandtl. The magnus effect and windpowered ships. *Naturwissenschaften*, 13:93–108, 1925.
- [32] P. H. Reisenthel, H. M. Nagib, and D. J. Koga. Control of separated flows using forced unsteadiness. In *AIAA paper 85-0556*, New York, 1985.
- [33] T. Sarpkaya. Vortex-induced oscillations. *J. Appl. Mech.*, 46:241–258, 1979.
- [34] S. S. Sritharan. An optimal control problem in exterior hydrodynamics. In E. B. Lee, G. Chen, L. Markus, and W. Littman, editors, *New Trends and Applications of Distributed Parameter Control Systems*, pages 385–417. Marcel Dekker, 1990.
- [35] S. S. Sritharan. Dynamic programming of the Navier-Stokes equations. *Systems and Control Letters*, 16:299–307, 1991.



- [36] S.S. Sritharan, Y.R. Ou, J.A. Burns, D. Ladd, E. Hendrick, and N. Nossier. Optimal control of viscous flow past a cylinder: mathematical theory, computation and experiment. I. Submitted to Quarterly of Applied Mathematics, 1992.
- [37] W. M. Swanson. The Magnus effect: a summary of investigations to date. *ASME J. Basic Engrg.*, 83:461-470, 1961.
- [38] S. Taneda. Visual study of unsteady separated flows around bodies. *Prog. Aero. Sci.*, 17:287-348, 1977.
- [39] S. Taneda. Visual observations of the flow past a circular cylinder performing a rotatory oscillation. *J. Phys. Soc. Japan*, 45:1038-1043, 1978.
- [40] P. T. Tokumaru and P. E. Dimotakis. Rotary oscillation control of a cylinder wake. *J. Fluid Mech.*, 224:77-90, 1991.
- [41] A. Wambecq. Rational Runge-kutta methods for solving systems of ordinary differential equations. *Computing*, 20:333-342, 1978.
- [42] C. H. K. Williamson. Sinusoidal flow relative to circular cylinders. *J. Fluid Mech.*, 155:141-174, 1985.
- [43] C. H. K. Williamson. Defining a universal and continuous Strouhal-Reynolds number relationship for the laminar vortex shedding of a circular cylinder. *Phys. Fluids*, 31:2742-2744, 1988.
- [44] C. H. K. Williamson and A. Roshko. Vortex formation in the wake of an oscillating cylinder. *J. Fluids and Structures*, 2:355-381, 1988.
- [45] J. C. Wu. Numerical boundary conditions for viscous flow problems. *AIAA J.*, 14:1042-1049, 1976.

- [46] J. C. Wu and J. F. Thompson. Numerical solutions of time-dependent incompressible Navier-Stokes equations using an integral-differential formulation. *Computers & Fluids*, 1:197-215, 1973.

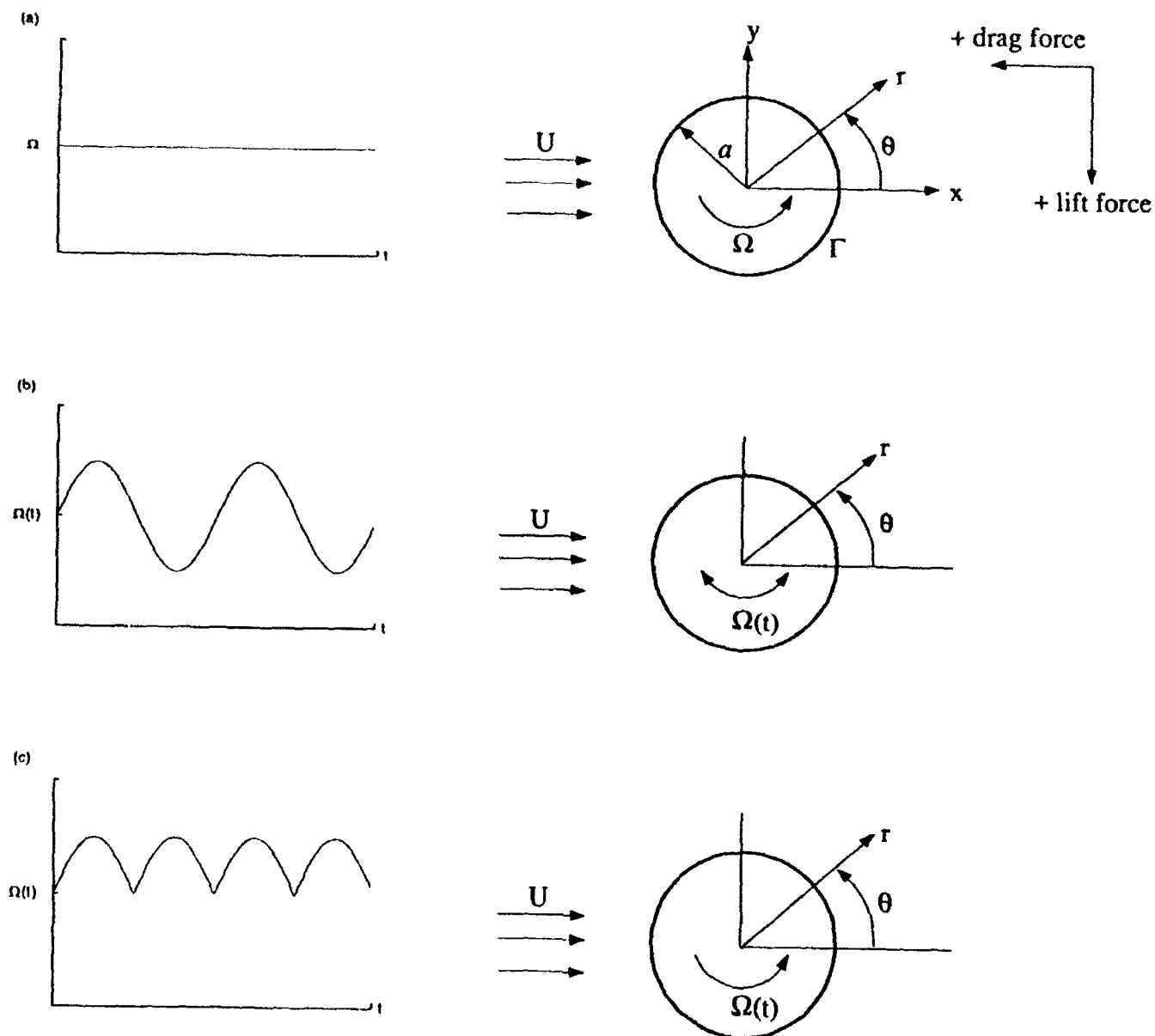


**FIGURE 1:** Schematic of the rotating cylinder with three types of rotation: (a)  $\alpha(t) = a\Omega(t)/U = \text{constant}$ ; (b)  $\alpha(t) = A \sin \pi Ft$ ; (c)  $\alpha(t) = A |\sin \pi(F/2)t|$ .

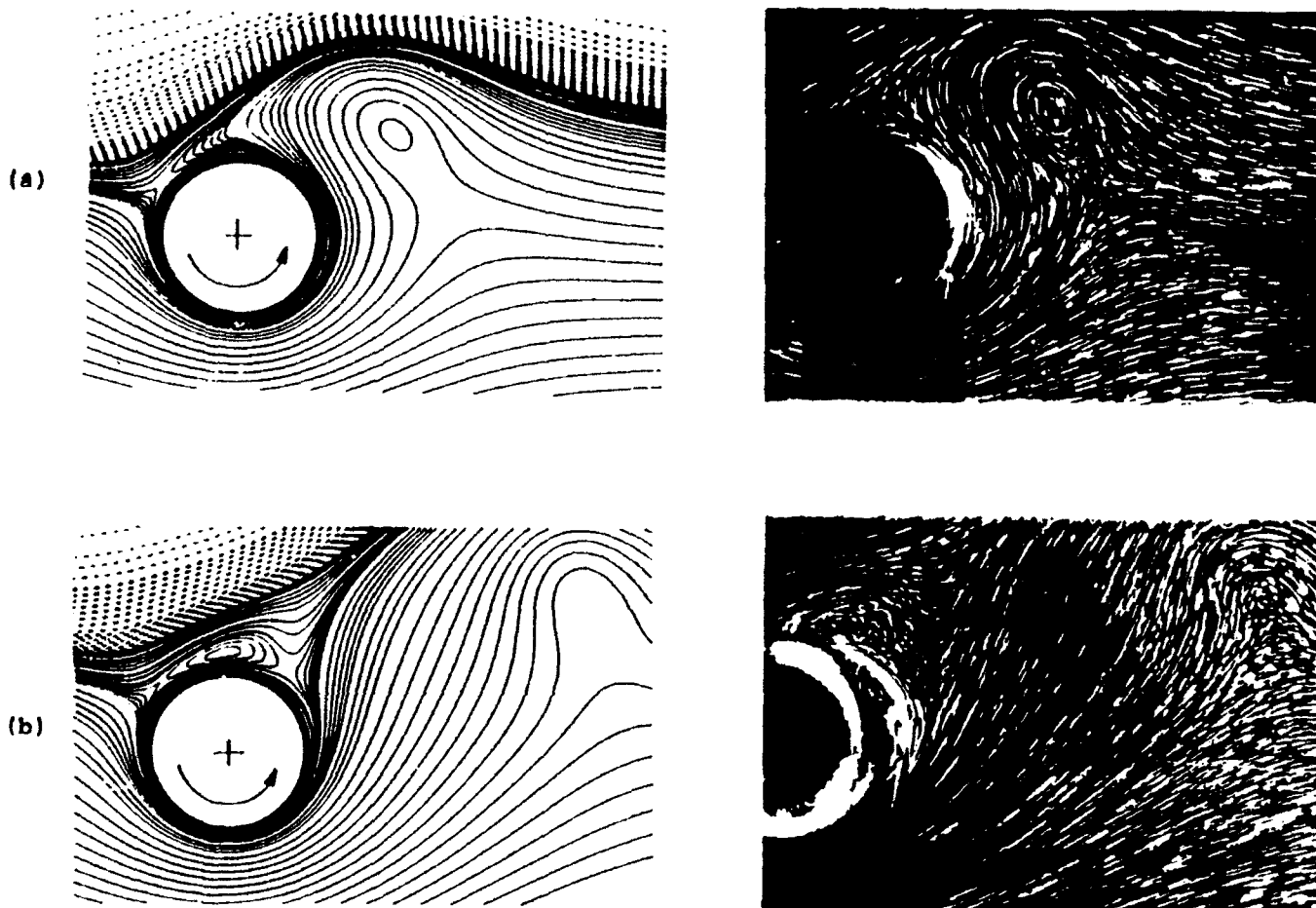


**FIGURE 2:** Instantaneous streamlines plots for  $Re = 200, \alpha = 2.07$  at (a)  $t = 5.0$ , (b)  $t = 9.0$ : computed (left); flow-visualization pictures (right).

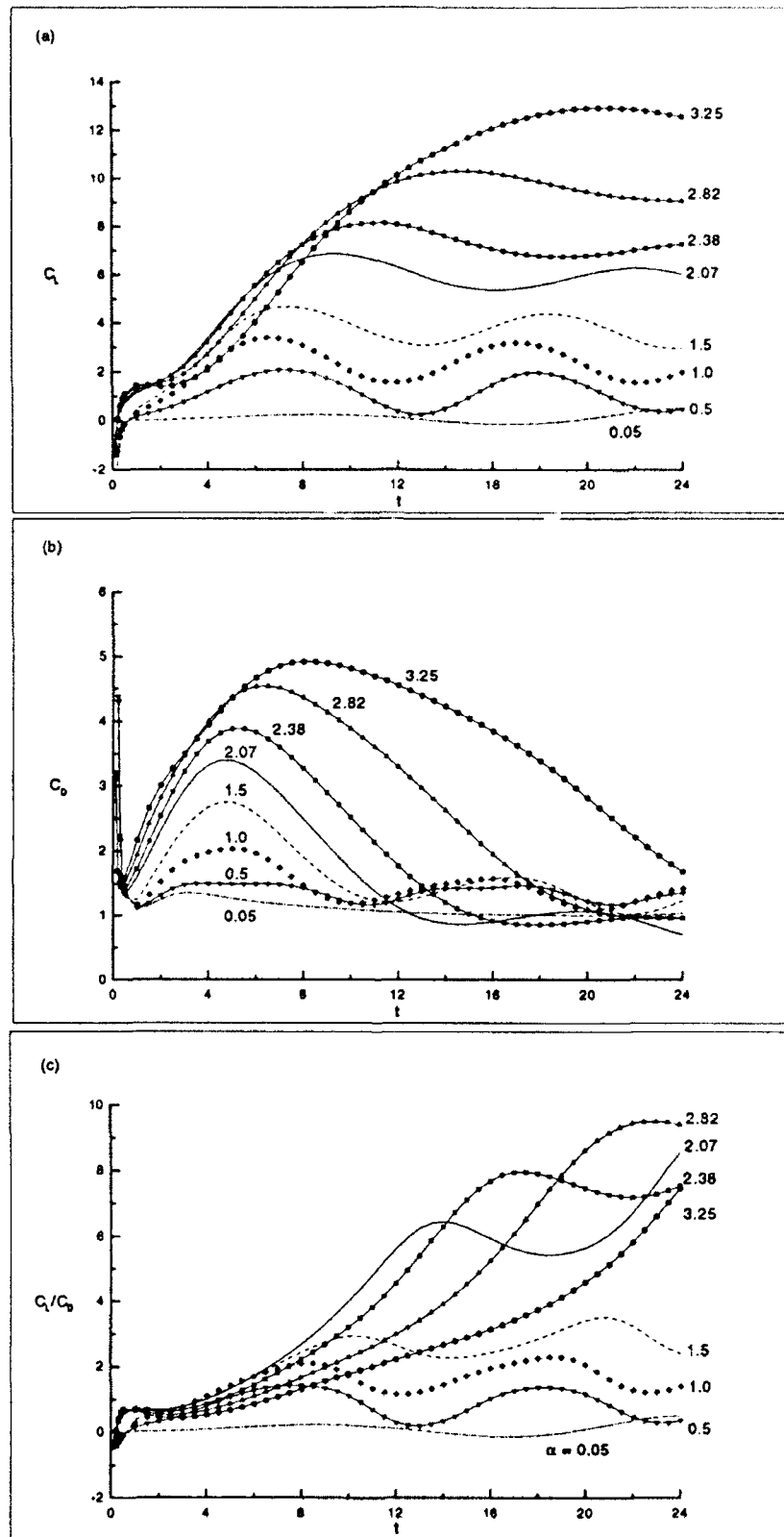


**FIGURE 3:** Temporal evolution of the lift (a), drag (b) and lift/drag (c) coefficients at  $Re = 200$  with various constant speed ratios ( $0.05 \leq \alpha \leq 3.25$ ).

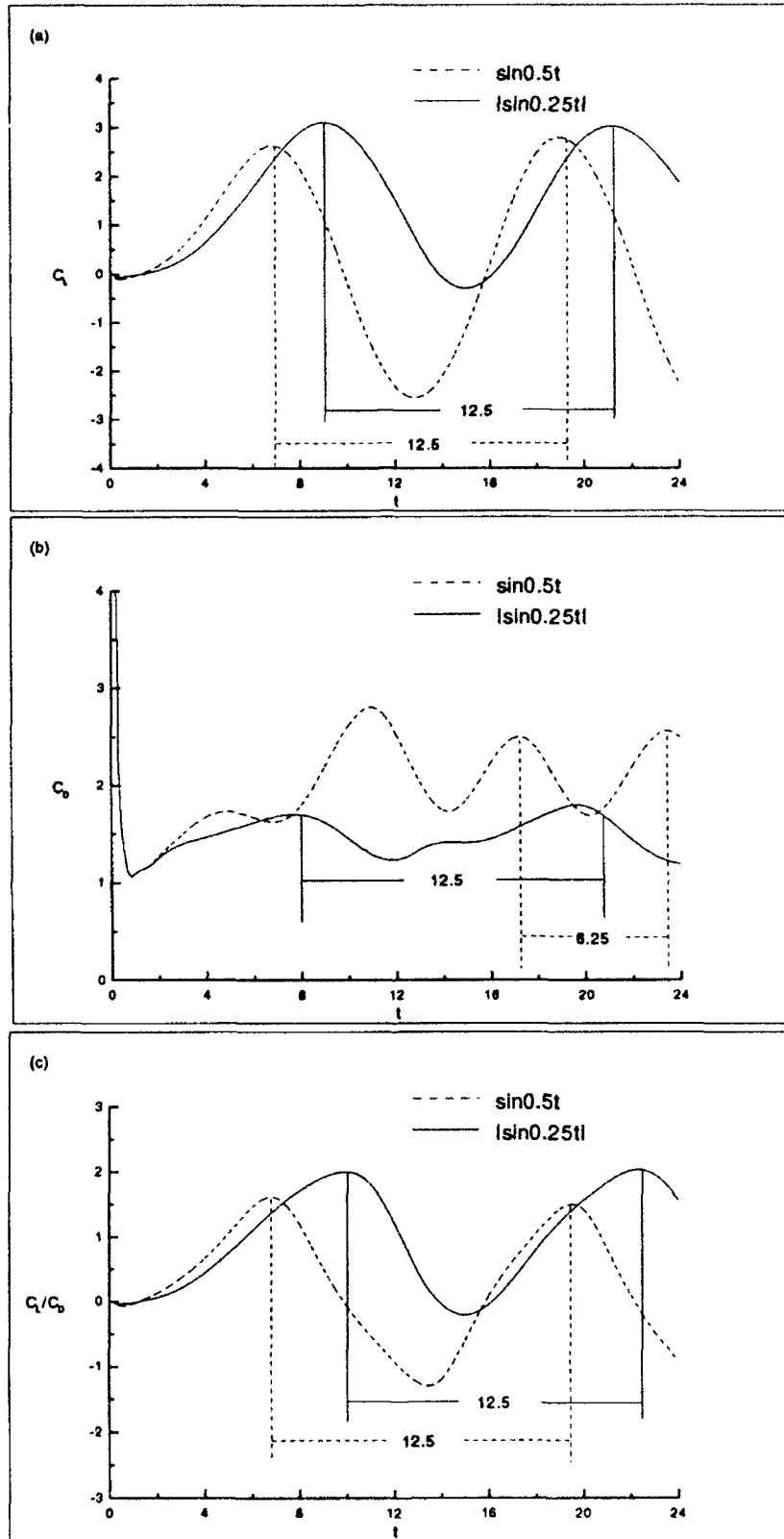


**FIGURE 4:** Comparison of temporal evolution of the lift (a), drag (b) and lift/drag (c) coefficients for a time-periodic rotation  $\alpha(t) = |\sin 0.25t|$  ( $T = 12.5$ ) with a time-harmonic rotary oscillation  $\alpha(t) = \sin 0.5t$  ( $T = 12.5$ ) at  $Re = 200$  for  $0 \leq t \leq 24$ .

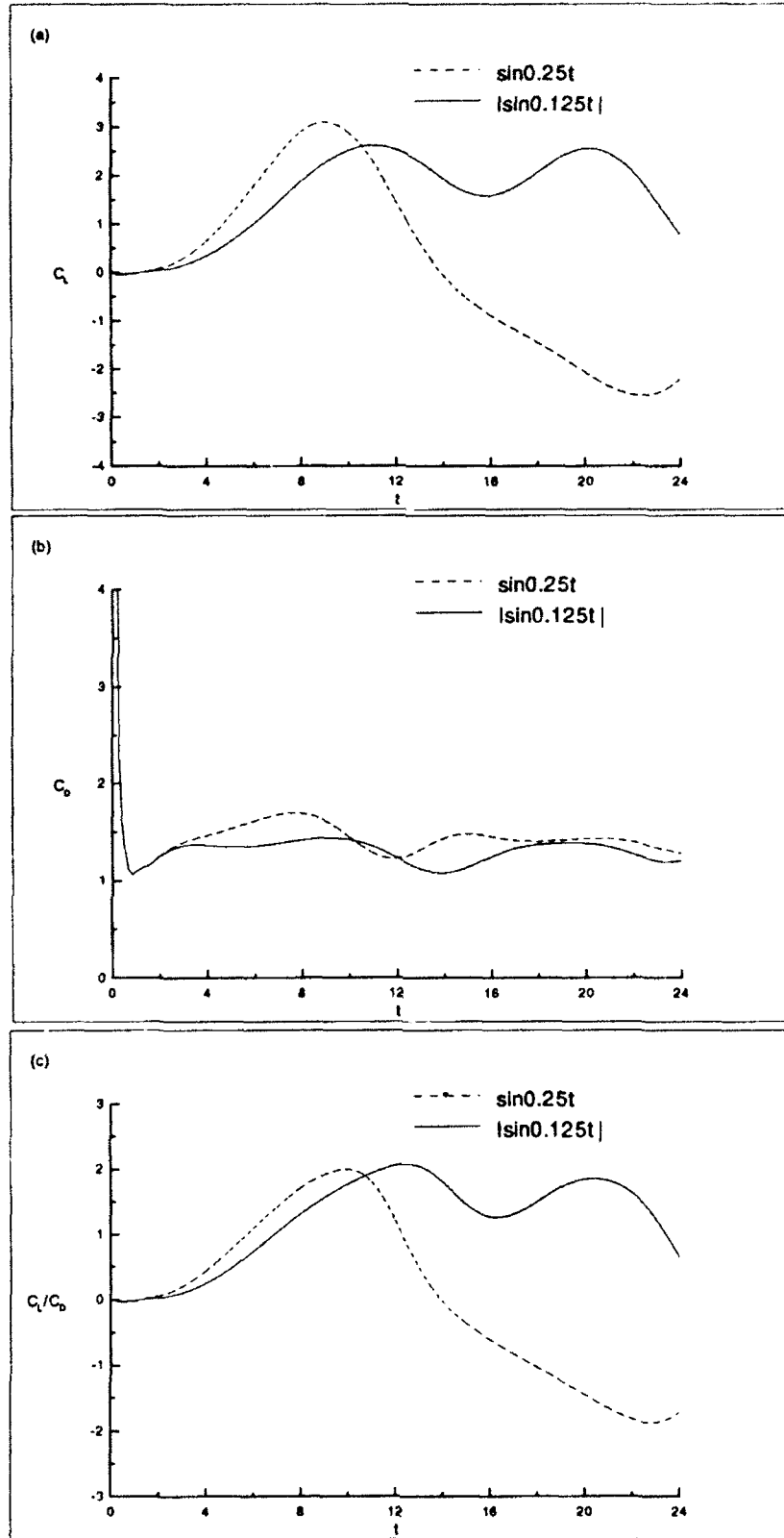


**FIGURE 5:** Comparison of temporal evolution of the lift (a), drag (b) and lift/drag (c) coefficients for a time-periodic rotation  $\alpha(t) = |\sin 0.125t|$  with a time-harmonic rotary oscillation  $\alpha(t) = \sin 0.25t$  at  $Re = 200$  for  $0 \leq t \leq 24$ .

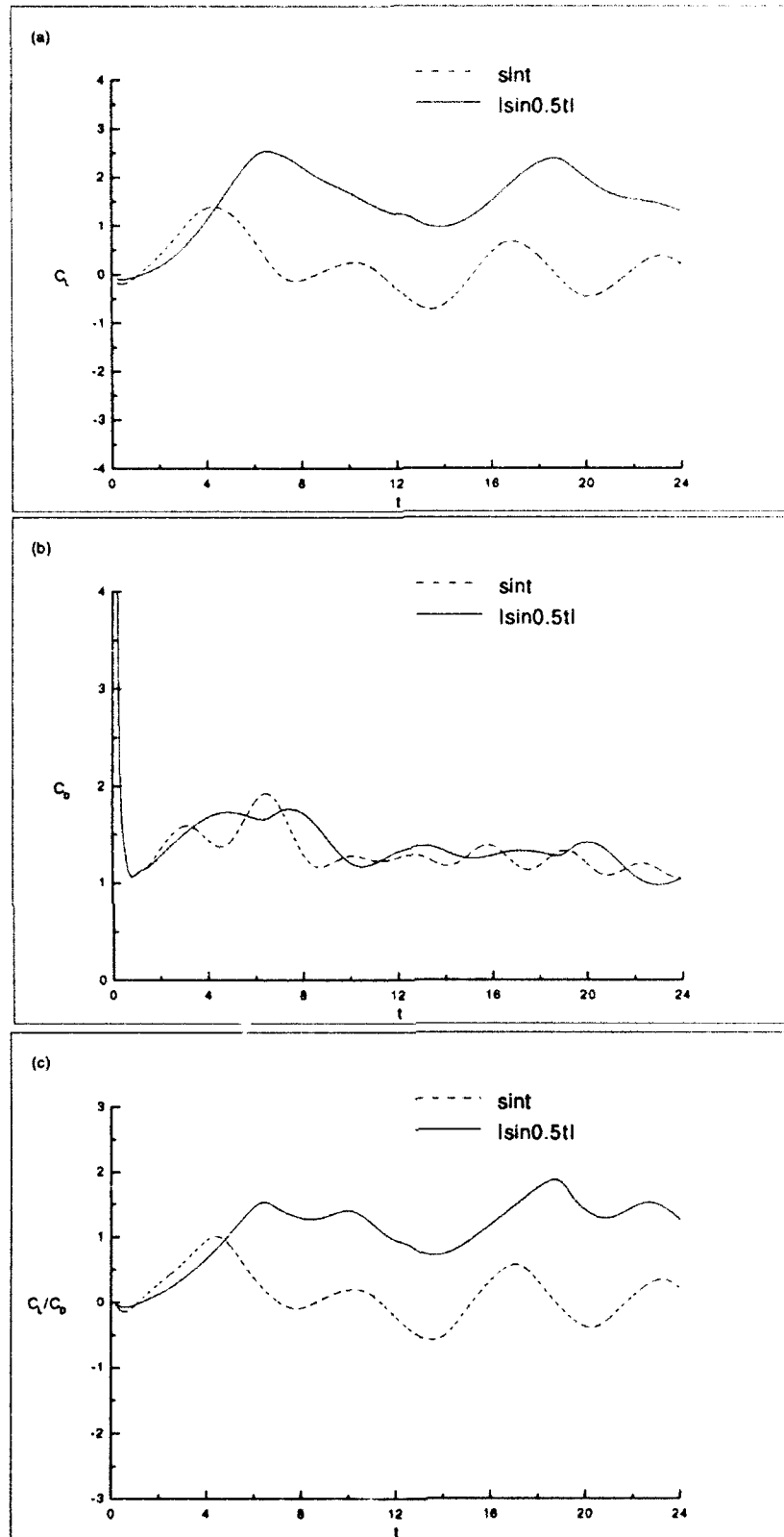


**FIGURE 6:** Comparison of temporal evolution of the lift (a), drag (b) and lift/drag (c) coefficients for a time-periodic rotation  $\alpha(t) = |\sin 0.5t|$  with a time-harmonic rotary oscillation  $\alpha(t) = \sin t$  at  $Re = 200$  for  $0 \leq t \leq 24$ .



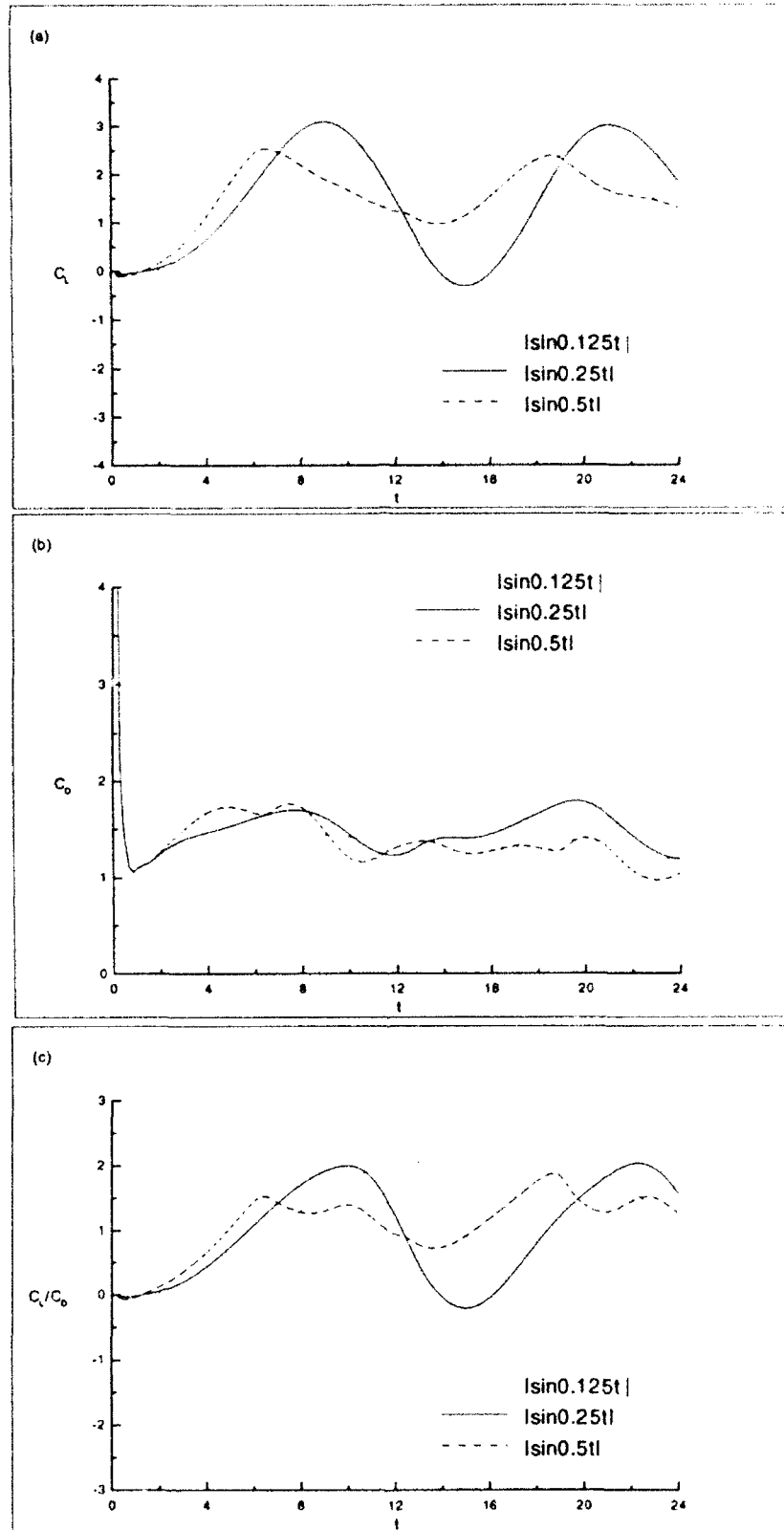


**FIGURE 7:** Temporal evolution of the lift (a), drag (b) and lift/drag (c) coefficients for a time-periodic rotation  $\alpha(t) = |\sin \pi(F/2)t|$  at  $Re = 200$  with various forcing frequencies of  $F = 0.08, 0.16$  and  $0.32$  for  $0 \leq t \leq 24$ .

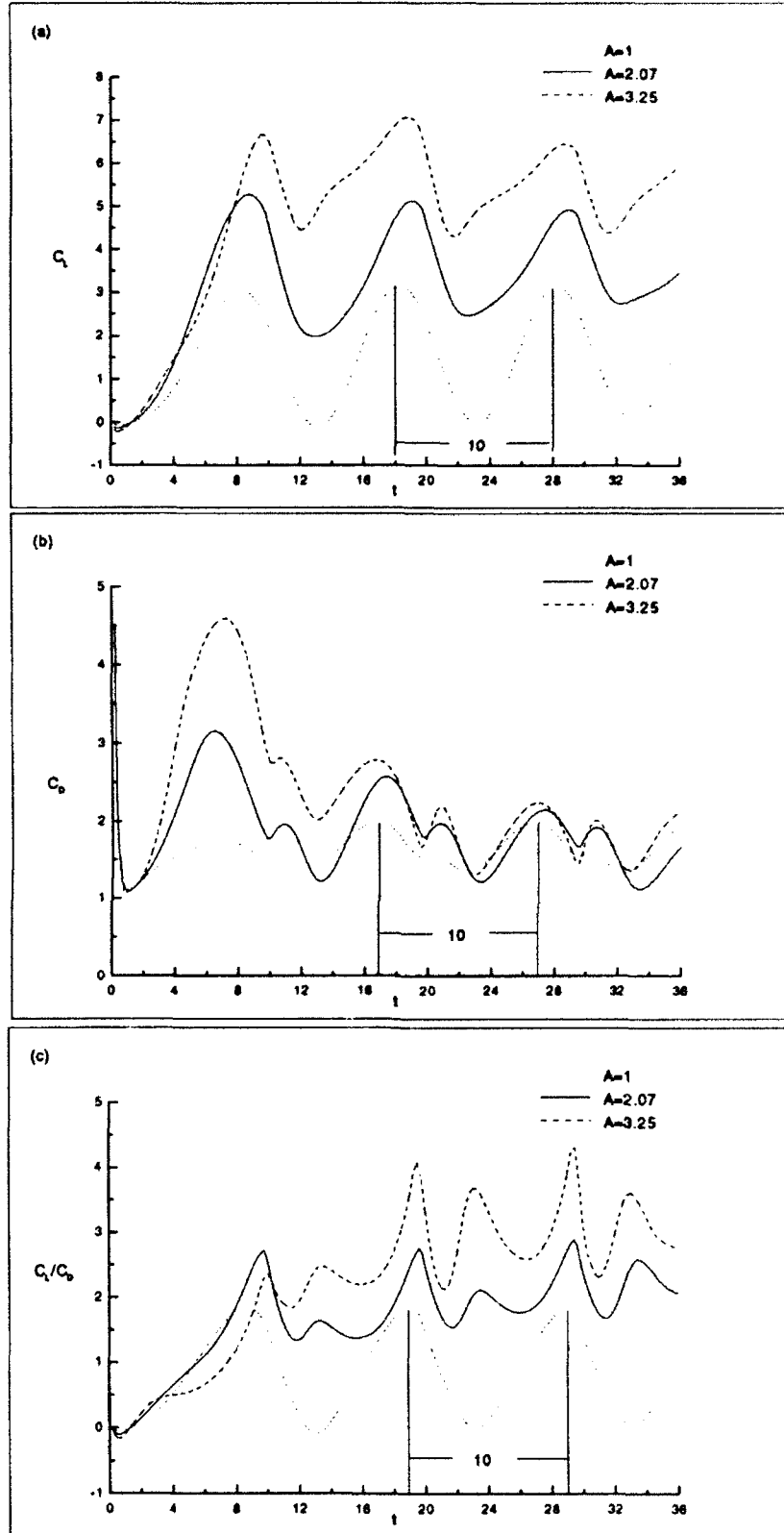


**FIGURE 8:** Temporal evolution of the lift (a), drag (b) and lift/drag (c) coefficients for a time-periodic rotation  $\alpha(t) = A|\sin 0.314t|$  at  $Re = 200$  with various amplitudes of  $A = 1.0, 2.07$  and  $3.25$  for  $0 \leq t \leq 36$ .

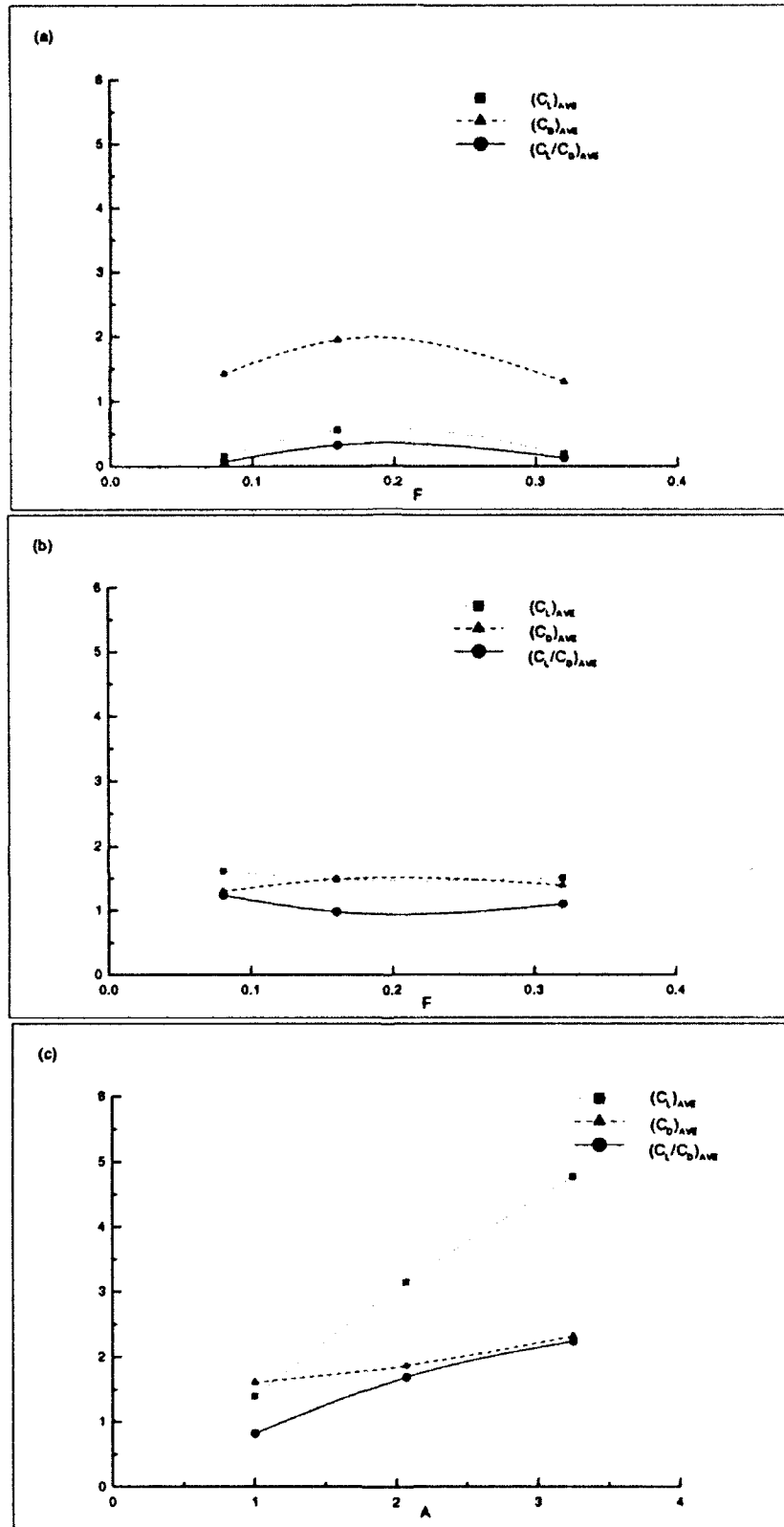


**FIGURE 9:** Variation of time-averaged forces coefficients with respect to the forcing frequency and the angular amplitude: (a)  $\alpha(t) = \sin \pi F t$  and  $0.08 \leq F \leq 0.32$ ; (b)  $\alpha(t) = |\sin \pi(F/2)t|$  and  $0.08 \leq F \leq 0.32$ ; (c)  $\alpha(t) = A|\sin 0.314t|$  and  $1 \leq A \leq 3.25$ .

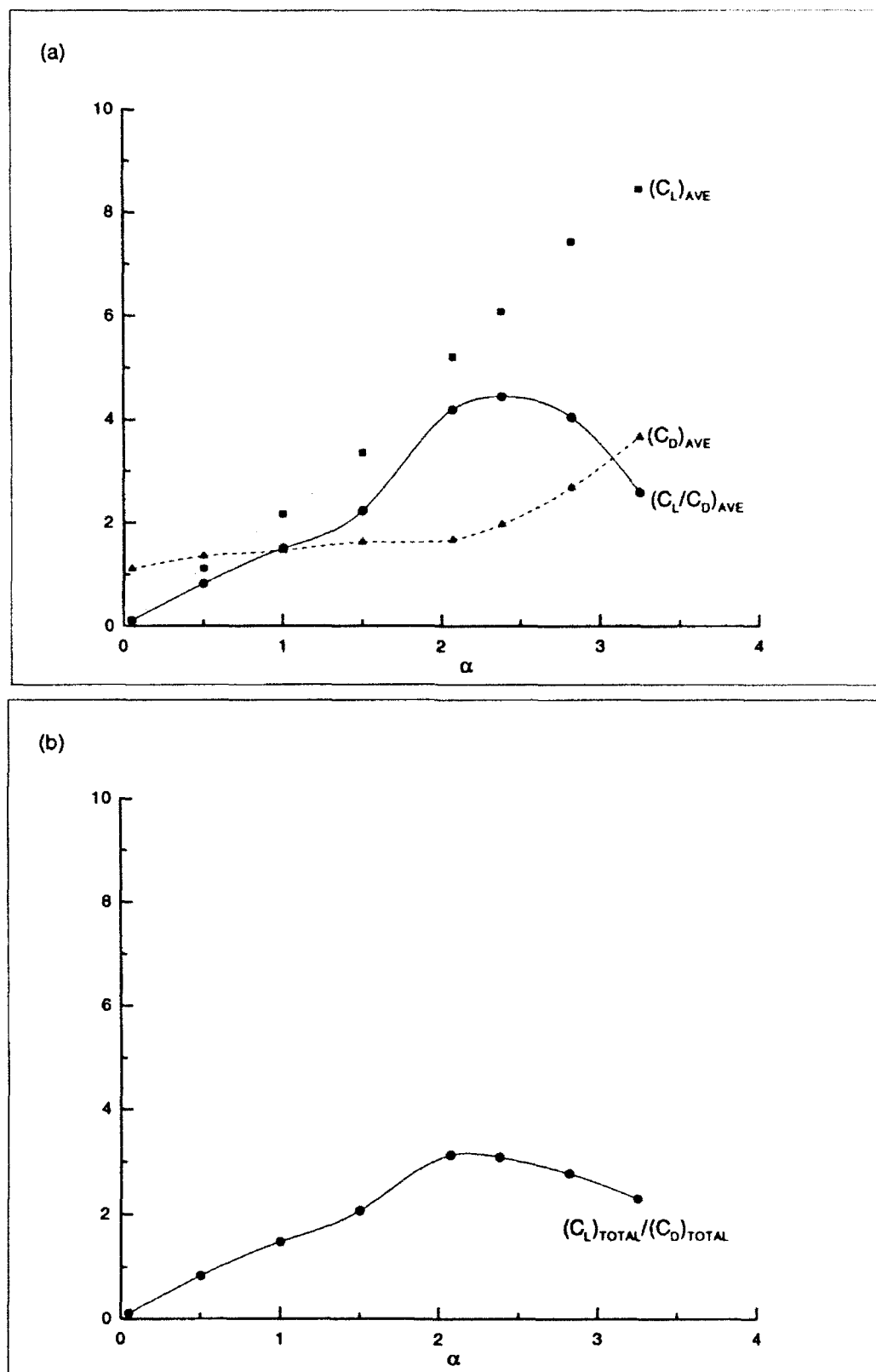


**FIGURE 10:** Effect of the speed ratio on time-averaged lift, drag and lift/drag coefficients (a) and on total lift/total drag force ratio (b) for  $0 < \alpha \leq 3.25$ .

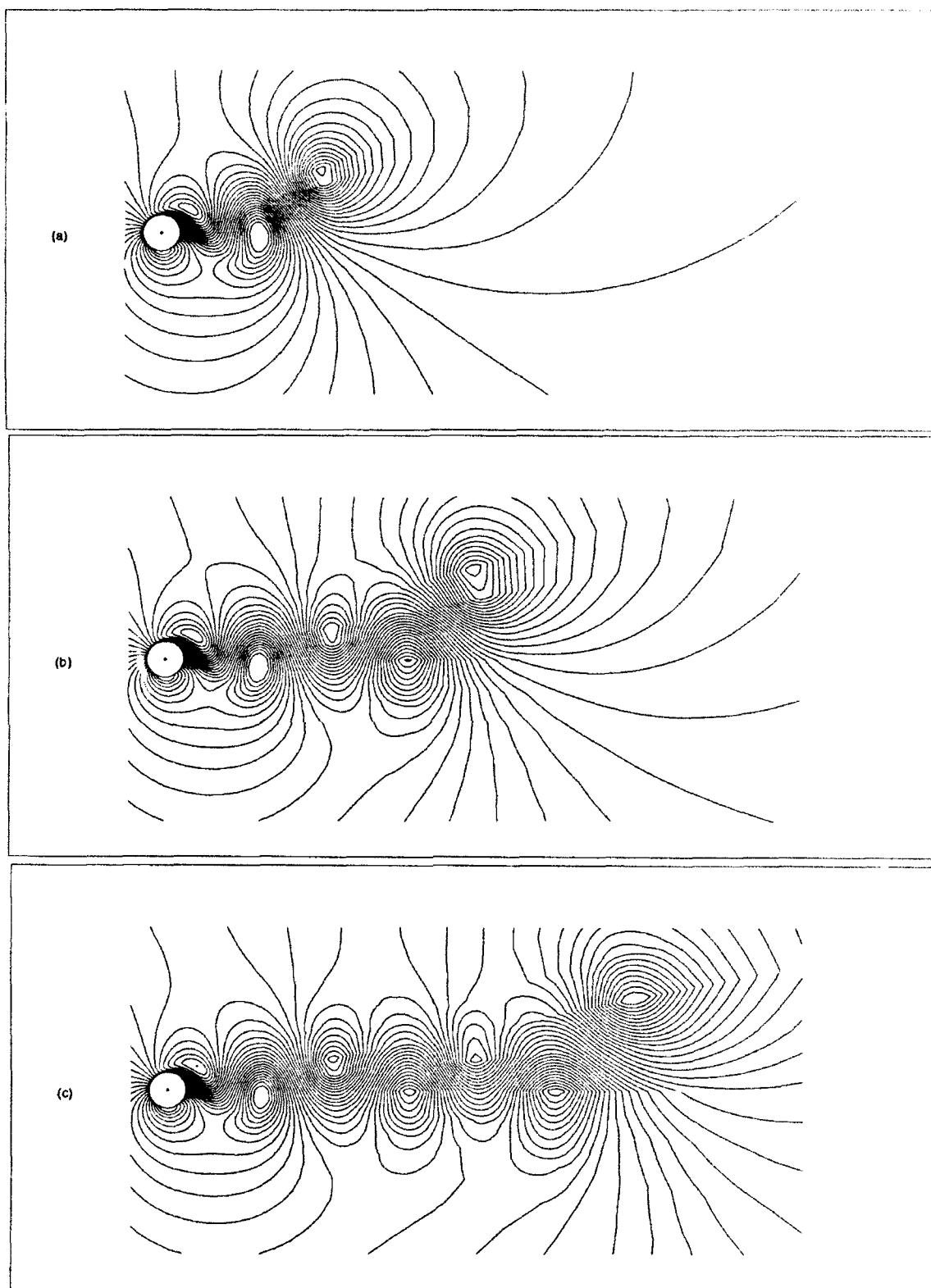


**FIGURE 11:** Instantaneous streamlines plots for  $Re = 200$ ,  $\alpha(t) = |\sin 0.314t|$  ( $F = 0.2$ ), viewed from a frame fixed with the undisturbed fluid. (a)  $t = 16$ , (b)  $t = 26$ , (c)  $t = 36$ .

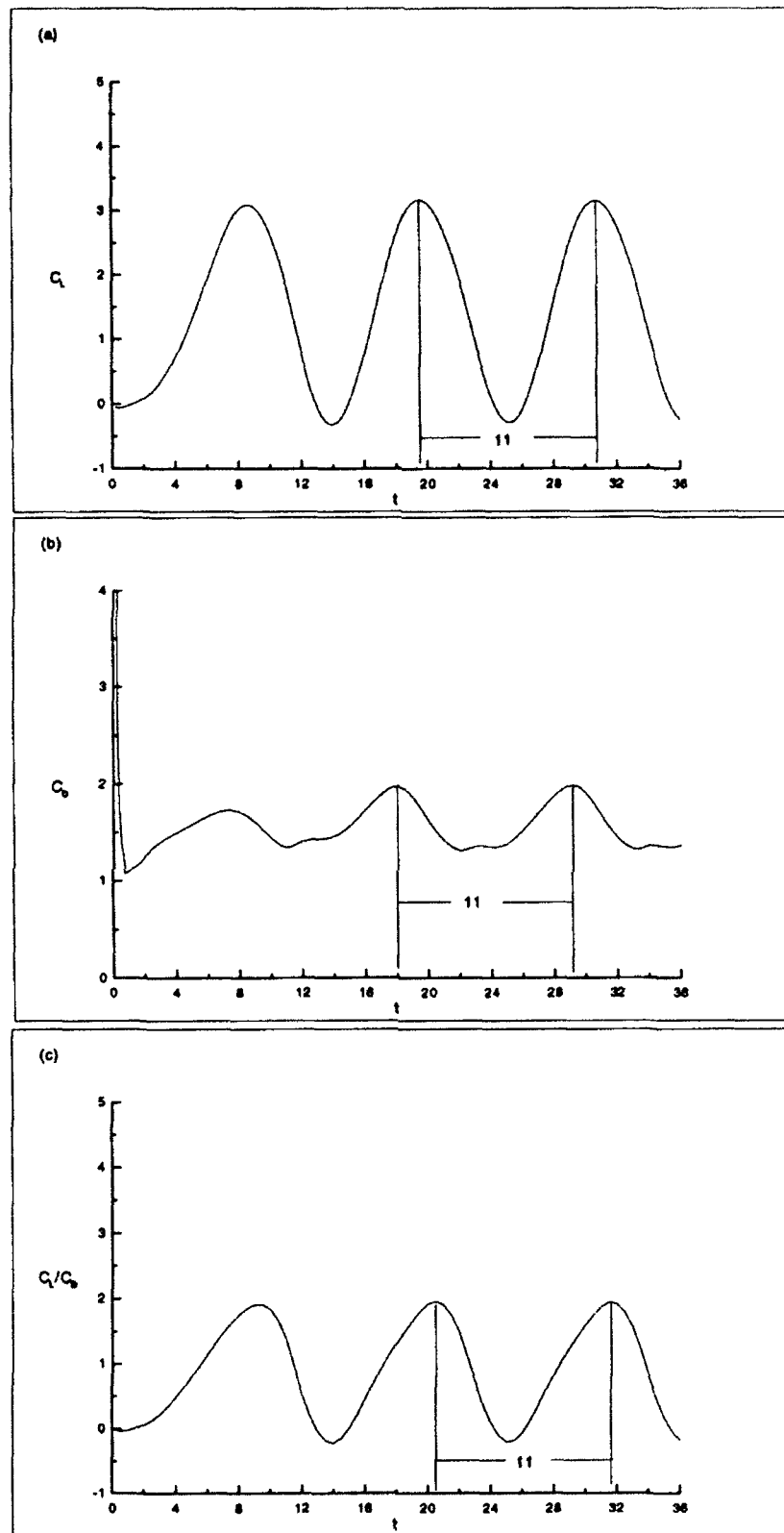


**FIGURE 12:** Temporal evolution of the lift (a), drag (b) and lift/drag (c) coefficients for a time-periodic rotation  $\alpha(t) = |\sin 0.283t|$  ( $F = 0.18$ ) at  $Re = 200$  for  $0 \leq t \leq 36$ .

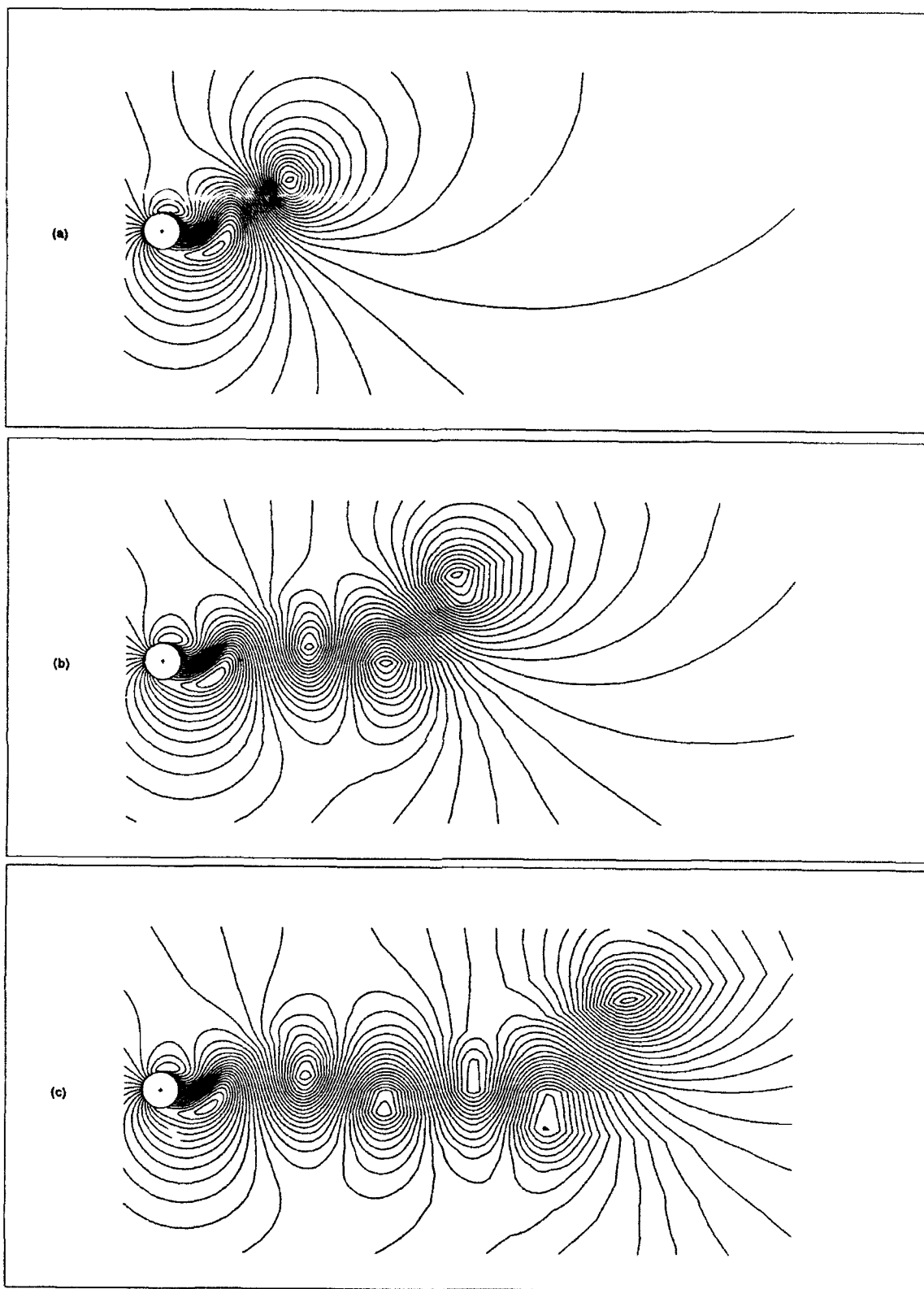


**FIGURE 13:** Instantaneous streamlines plots for  $Re = 200$ ,  $\alpha(t) = |\sin 0.283t|$  ( $F = 0.18$ ), viewed from a frame fixed with the undisturbed fluid. (a)  $t = 14$ , (b)  $t = 25$ , (c)  $t = 36$ .

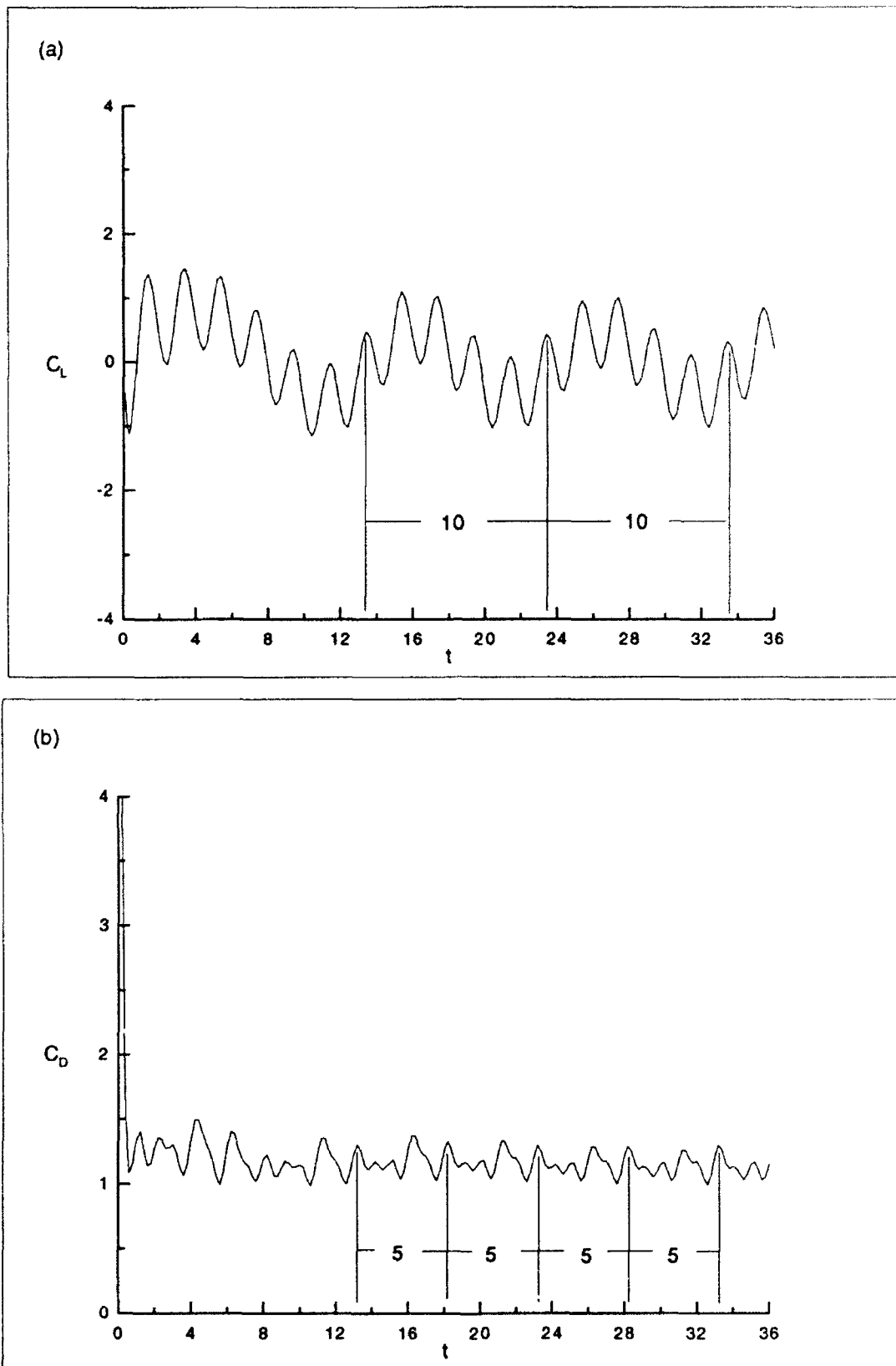


**FIGURE 14:** Temporal evolution of the lift (a) and drag (b) coefficients for a time-harmonic rotary oscillation  $\alpha(t) = 2 \sin 3.14t$  ( $F = 1.0$  and  $A = 2$ ) at  $Re = 200$  for  $0 \leq t \leq 36$ .



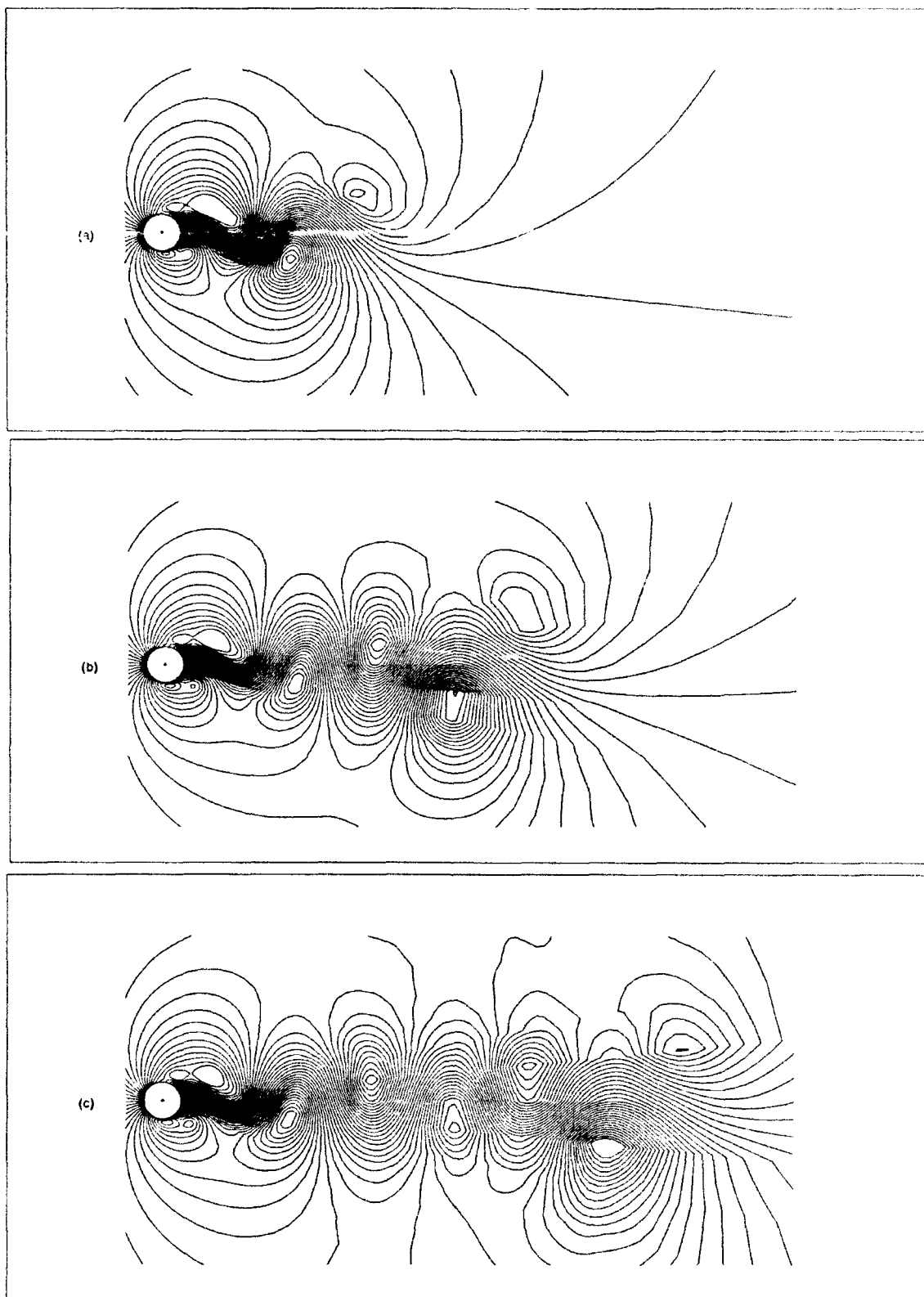


**FIGURE 15:** Instantaneous streamlines plots for  $Re = 200$ ,  $\alpha(t) = 2 \sin 3.14t$  ( $F = 1.0$  and  $A = 2$ ), viewed from a frame fixed with the undisturbed fluid. (a)  $t = 16$ , (b)  $t = 26$ , (c)  $t = 36$ .